Voltage Sensor Conformations Induced by LQTS-associated Mutations in hERG Potassium Channels

Aaron N. Chan[2], Co D. Quach[2], Lucas J. Handlin[1], Erin N. Lessie[1], Emad Tajkhorshid[2], and Gucan Dai[1,*]

Author Affiliations:

[1]Department of Biochemistry and Molecular Biology, Saint Louis University School of Medicine

[2]Theoretical and Computational Biophysics Group, NIH Center for Macromolecular Modeling and Visualization, Beckman Institute for Advanced Science and Technology, Department of Biochemistry, and Center for Biophysics and Quantitative Biology, University of Illinois at Urbana-Champaign

*Correspondence: gucan.dai@health.slu.edu

ABSTRACT

Voltage sensors are essential for electromechanical coupling in hERG K^+ channels, critical to cardiac rhythm. These sensors respond to membrane potential changes by moving within the transmembrane electric field. Mutations in hERG voltage-sensing arginines, associated with Long-QT syndrome, alter channel gating, though underlying mechanisms remain unclear. Using live-cell fluorescence lifetime imaging microscopy (FLIM), transition metal FRET (tmFRET), an improved dual stop-codon-mediated strategy for noncanonical amino-acid incorporation, and molecular dynamics (MD) simulations, we identified intermediate voltage-sensor conformations induced by neutralizing key arginines in the charge transfer center. Phasor plot analysis of FLIM data revealed multiple voltage-dependent FRET states in these mutants, in contrast to the single high-FRET state observed in controls. These intermediate FRET states reflect distinct conformations of the voltage sensor, corresponding to predicted structures of voltage sensors in MD simulations. This study provides novel insights into cardiac channelopathies, highlighting a structural mechanism that impairs voltage sensing in cardiac arrhythmias.

INTRODUCTION

Voltage sensing of ion channels is crucial for regulating cardiac and neuronal excitability[1]. Voltage sensors detect changes in membrane voltage, thereby initiating conformational changes that govern the opening and closing of voltage-gated ion channels (VGICs)[1,2]. This pivotal role allows VGICs to precisely control the flux of ions across cell membranes, thereby orchestrating essential physiological processes such as action potentials in neurons, muscle contraction, cardiac pacemaking, and secretion of neurotransmitters. Notably, dysfunction of ion channels is implicated in various disease states, including the prolonged QT-interval syndrome (long QT syndrome, LQTS), a cardiac disorder characterized by prolonged ventricular repolarization, which can cause life-threatening arrhythmias. Mutations in the human *ether-à-go-go*-related gene (hERG), which encodes the cardiac potassium channel Kv11.1, represent a prevalent cause of congenital LQTS[3,4]. The hERG channel, belonging to the voltage-gated ion channel (VGIC) superfamily, features a functional voltage sensor, where mutations linked to LQTS have been identified[5].

Voltage sensors of VGICs are characterized by repeats of positively charged arginines within the 4th transmembrane helix (S4), which directly sense the transmembrane electric field[2]. The function of the S4 relies on its significant "up and down" movements within the voltage-sensing domain (VSD)[2,6-13]. These movements are central to electromechanical coupling, the process by which electrical changes across the membrane are converted into mechanical motions that open or close the channel pore. In hERG channels, the S4 helix is part of a conserved VSD (S1–S4 helices) and connects to the pore domain (PD; S5–S6 helices) through a short S4-S5 linker[14]. A cryo-EM structure has captured hERG in a conformation with the S4 in the up position and the pore in an open state[14]; however, other conformational states remain largely uncharacterized. While hERG shares a general domain architecture with other VGICs, it also displays distinct features, including a non-domain-swapped VSD–PD arrangement and potential modulation by intracellular regions such as the N-terminal Per-Arnt-Sim (PAS) domain and the C-terminal C-linker/cyclic nucleotide-binding homology domain (CNBHD)[14,15].

The conformational dynamics of the S4 helix—particularly the elusive down state at hyperpolarized voltages—are critical for understanding voltage sensing in VGICs. High-resolution structures of the S4 in its up-state conformation were first captured in the absence of voltage difference (0 mV)[2,16,17]. In comparison, capturing the down state, which corresponds to the S4 voltage sensor at hyperpolarized membrane potentials, has been notably more challenging. This down conformation was first observed in an *Arabidopsis* two-pore channel (TPC)[7]. Similar down conformations have been identified in other VGICs such as voltage-gated sodium channels and pacemaker hyperpolarization-

activated cyclic nucleotide-gated (HCN) channels[8-11,18]. Furthermore, cryo-electron microscopy (cryo-EM) studies have provided atomic-level insights into voltage sensors under hyperpolarizing conditions. This was achieved by reconstituting the channels into liposome membranes and manipulating ionic gradients to apply hyperpolarizing voltages, an approach that requires the channel pores to remain closed to prevent ion leakage across the membrane[12,13]. This approach has yielded cryo-EM structures of ether-à-go-go (Eag) channels, a close relative of hERG, in multiple conformational states including up, down, and intermediate forms[12]. However, studying the conformational dynamics and heterogeneity of these S4 voltage-sensor states under native membrane environments remains a significant challenge. A more comprehensive understanding of the structural dynamics and potential multi-step movements of the voltage sensor is crucial for elucidating the electromechanical coupling governing VGIC function.

While fluorescence imaging stands as a valuable tool for understanding the structural mechanisms of voltage sensors, significant technical hurdles arise in controlling membrane voltage for such imaging experiments. Single-molecule fluorescence techniques hold promise, with their capacity to discern distinct protein conformational states, yet their application in probing the voltage-dependent structural arrangements of VGICs remains limited in a native membrane[19,20]. Understanding the structure-function relationship of VGICs often necessitates live-cell imaging, particularly as voltage sensor dynamics depend on membrane lipids in their native environments. However, traditional intensity-based ensemble methods average signals across molecules, often obscuring conformational heterogeneity. In contrast, fluorescence lifetime imaging microscopy (FLIM), especially when combined with transition metal ion FRET (tmFRET), can distinguish structural states based on fluorescence lifetime rather than intensity[21-24]. This study introduces a novel application of FLIM-tmFRET with site-specific incorporation of noncanonical amino acids (ncAAs) to monitor conformational dynamics of the S4 in live cells. Our approach enables high-resolution, state-specific measurements under near-native conditions, offering a significant advance in the structural study of voltage sensors within VGICs.

In this study, we employed a combination of techniques including dual stop-codon suppression-mediated incorporation of ncAAs for site-specific fluorescence labeling, phasor FLIM-tmFRET, and MD simulations to examine the impact of a LQTS-associated mutation on conformational rearrangements of hERG voltage sensors in transfected human cell lines. We identified structural alterations in hERG voltage sensors, including low-energy conformational intermediates, that underlie the functional effects of LQTS-associated mutations. This integrative approach offers a powerful and broadly applicable platform for quantitatively assessing the movements, conformational states, dynamics, and energetics of voltage sensors in ion channels.

RESULTS

Functional impact of S4 helix LQTS mutations on hERG channel activation

To investigate how specific charged residues in the S4 helix contribute to voltage sensing and gating in hERG channels, we focused on a subset of mutations previously implicated in LQTS. The hERG (K_v11.1 or KCNH2) channels expressed in tsA-201 cells exhibit a depolarization-dependent activation profile like other voltage-gated potassium channels[1]. Within the S4 helix of hERG, six positively charged arginines or lysines are present, with the arginines within the charge transfer center presumably serving as the primary voltage-sensing residues[25] (Supplementary Fig. 1a). Notably, most of these charged residues have been implicated in LQTS[5,26,27] (Supplementary Fig. 1a).

Homology models of hERG were generated using SWISS-MODEL, guided by previous cryo-EM studies that identified three distinct conformations of the voltage sensor in the rat Eag channel[12,28]. In the down state model at hyperpolarized voltages (Supplementary Fig. 1b), only the side chain of K525 of hERG is positioned above the "phenylalanine cap", F463, at the hydrophobic constriction site[25]. Upon membrane depolarization, the side chains of K525, R528, and R531 are predicted to relocate above the phenylalanine cap. In comparison, in the model of the hypothetical intermediate state, the side chains of K525 and R528, but not that of the R531, are positioned above the phenylalanine cap. This intermediate conformation may represent a transitional step during voltage sensor movement in hERG channels.

We examined the functional consequences of charge-neutralizing mutations in the context of the non-inactivating S620T background. In the presence of 10 mM tetraethylammonium (TEA) to fully inhibit endogenous potassium currents in tsA cells[29] (Supplementary Fig. 1c) - different from the wild-type (WT+; with S620T) hERG channels[30] - hERG channels with LQTS-associated mutation R531Q (R531Q+; also with S620T) demonstrated a noticeable initial phase of approximately 100 ms, preceding the delayed second phase (Fig. 1a). The activation profile was plotted using the instantaneous "tail current" amplitudes at -100 mV during repolarization at the end of the voltage protocol (Fig. 1a and b). The S620T mutation, near the selectivity filter, abolishes C-type inactivation in hERG channels, thereby enabling analysis of channel activation independently of the inactivation[30-32]. In this context, tail current amplitudes recorded from R531Q+ mutant channels revealed a substantial rightward shift in the conductance-voltage (G-V) relationship compared to wild-type channels (Fig. 1b); the voltage for the half maximal activation of R531Q+ channels was +81 ± 3.7 mV (n = 4) compared to +35 ± 2.8 mV (n = 8) for the WT+ channel. This large ~45 mV shift in the G-V and the biphasic channel activation are consistent with prior research

and indicative of potential intermediate states of the S4[26,33,34]. Furthermore, this initial lag was less noticeable in hERG-R528Q+ (with S620T) channels, followed by a double-exponential main current phase for the activation; the deactivation was much slower (Supplementary Fig. 1d)[35]. The R528Q mutation did not significantly shift the G-V relationship ($V_{1/2}$ = + 24 ± 7.7 mV, n = 4) compared to the WT+ and has not been linked to LQTS. Additionally, LQTS-linked mutation R534L (with R534Q also tested) produced hERG channels that have diminished multi-phasic activation kinetics. Instead, these channels exhibited considerable voltage-induced channel inactivation, despite the elimination of C-type inactivation by the S620T mutation (Supplementary Fig. 1e). Collectively, assessing the functional impact of these three charge-neutralization mutations on channel activation, the R531Q produces the most significant effect. This result is consistent with the finding that R531 is the primary residue that contributes to the total gating charge of 1.5 elementary electronic charges per subunit—a value notably smaller than that of classical voltage-gated potassium channels[33,36,37].

Measuring the movement of voltage sensors in hERG channels using FLIM-tmFRET

To directly visualize conformational changes in the VSD of hERG channels and assess how LQTS mutations affect these dynamics, we implemented a dual stop-codon suppression strategy to incorporate noncanonical amino acids for site-specific fluorescence labeling and FRET measurements of voltage-sensor movements[38]. We modified a human hERG1 construct by introducing amber (TAG) and ochre (TAA) stop codons at selected positions within the voltage-sensing domain (VSD) of hERG channels (Fig. 1). The amber stop-codon suppression approach facilitated the incorporation of a fluorescent noncanonical amino acid L-acridonyl-alanine (Acd) into the S4 helix[39,40]. This was achieved using a recently developed Acd tRNA/tRNA synthetase system adapted from the pyrrolysyl-tRNA synthetase of the archaeon *Methanomethylophilus alvus (M. alvus)* [40] (Fig. 1c). Importantly, this orthogonal strategy operates independently of the ochre stop-codon suppression system, which is derived from the pyrrolysyl-tRNA synthetase of the *Methanosarcina* archaea *M. mazei*/*M. barkeri*[41]. Specifically, we used a tRNA (M15-PylT)/PylRS pair derived from *M. mazei*/*M. barkeri* to introduce N-propargyl-L-lysine (ProK) into another relatively immobile site within the VSD. ProK features an alkyne group capable of undergoing specific chemical reactions with azide-containing compounds via copper(I)-catalyzed azide-alkyne cycloaddition (CuAAC) click chemistry. Previously, we have applied a similar approach to perform FLIM-tmFRET experiments for HCN channels[38,41], with the integration of Acd marking a notable enhancement over our prior dual stop-codon suppression methodology. Furthermore, this protein labeling design circumvents the necessity for cysteine-based labeling, mitigating potential concerns of mutating endogenous cysteine residues (~160) within hERG channels.

We designed a tmFRET pair comprising Acd as the FRET donor and Cu^{2+} chelated by 1,4,7,10-tetraazacyclododecane-1,4,7,10-tetraacetic acid (DOTA) as the FRET acceptor. The emission spectrum of Acd overlaps with the absorption spectrum of Cu^{2+} or Co^{2+} coordinated by an azido mono-amide-DOTA (Fig. 1d). The weak molar absorption of transition metals results in a shorter Förster distance (R_0 = ~ 10 – 20 Å, depending on the exact design) for tmFRET compared to conventional FRET pairs[23,24,42-44]. This reduced working distance of tmFRET is well-suited for investigating voltage-sensor movement in ion channels[10,11,38,45]. For probing the S4 movement of hERG channels, we positioned the Acd site at the L523 position near the N-terminal side of the S4 helix and the ProK/Cu^{2+}-DOTA site at the G439 position at the C-terminal end of the S1 helix (Fig. 1e). This design is predicated on the premise that the FRET donor and acceptor should be distant enough when the S4 is in the down state, resulting in minimal FRET, and exhibit increased FRET when they approach due to membrane depolarization. Because of the short R_0 of this tmFRET pair, FRET occurs primarily within the same subunit; inter-subunit FRET is negligible[10,11,38]. Additionally, this hERG construct—designated $hERG_{tmFRET}$ and containing the mutations G439TAA, L523TAG, and S620T—includes a C-terminal YFP tag to indicate the expression of full-length proteins at the cell membrane. Our observations revealed a correlation between YFP fluorescence and Acd fluorescence, confirming the expression of hERG channels (Supplementary Fig. 2). Functionally, for hERG channels with Acd and ProK incorporated ($hERG_{tmFRET}$ construct), similar depolarization-dependent activation was observed, with R531Q significantly rightward shifted the G-V relationship compared to the control (Supplementary Fig. 2).

Phasor FLIM was used to quantify the tmFRET by measuring the lifetime of Acd in tsA cells. One advantage of Acd is its exceptionally long and mono-exponential lifetime (~16 ns free in solution and ~12 ns when incorporated in cells)[23]. Both time-domain and frequency-domain types of FLIM were performed, which yielded similar lifetime values for the membrane-localized fluorescence coming from the Acd incorporated at the L523 position of the S4 helix (Fig. 1f). In frequency-domain FLIM analysis, lifetime data from each pixel of the confocal image are mapped onto a phasor plot—a complex plane where the universal semicircle serves as a reference for fluorescence lifetimes (Fig. 1f)[21,46,47]. Following Fourier transformation, the x-axis represents the real (G) component, and the y-axis represents the imaginary (S) component of the fluorescence decay. Pixels corresponding to mono-exponential lifetimes fall precisely on the semicircle, whereas multi-exponential decays localize within it. Importantly, shorter lifetimes are positioned further clockwise along the semicircle. Accounting for minor background contributions, the measured Acd phasor in cells localizes close to the semicircle, indicating a near mono-exponential decay, which facilitates our subsequent FRET analysis.

We used the FRET trajectory function facilitated by the phasor approach of FLIM to assess the change in tmFRET, comparing tsA cells expressing hERG channels imaged in either regular phosphate-buffered saline (PBS) or a depolarizing solution containing 120 mM KCl (Fig. 2 g-i). This function relies on the concept that the degree of shortened donor lifetime reports FRET efficiency, thereby representing the distance between the FRET donor and acceptor. The FRET trajectory starts from zero FRET efficiency, aligning with the donor-alone reference, and follows a path through the measured phasor species, ending at the theoretical 100% FRET efficiency at the origin (0, 0) coordinate, where most of the background noise is situated (Supplementary Fig. 2b and Supplementary Fig. 3a). For $hERG_{tmFRET}$ channels, FRET efficiency was minimal in PBS as expected but increased upon exposure to 120 mM KCl. In addition, treatment of 120 mM KCl did not affect the lifetime of the Acd donor alone. Conversely, in comparison to the $hERG_{tmFRET}$, the presence of R531Q produced a similarly low FRET efficiency in PBS, but the increase in FRET after the high KCl was attenuated (Fig. 1i). This outcome corresponds to the rightward shift observed in the G-V curve of the hERG-R531Q+ channels, indicating a compromise in the extent or likelihood of voltage sensor movement.

However, while the FRET trajectory method used in ensemble imaging experiments offers valuable insights, it also comes with limitations. Although it provides a quantified FRET efficiency, it only represents an averaged distance between donors and acceptors, lacking the capacity to reveal more detailed structural information and the conformational heterogeneity of the S4 helix (Supplementary Fig. 3a). As a result, this approach is insufficient for testing hypotheses about intermediate voltage sensor states or assessing how specific arginine mutations may influence distinct conformational states. To address these limitations, we employed an alternative strategy based on the principles of phasor addition and linear unmixing in phasor FLIM[21,47].

Probing the conformational heterogeneity of hERG voltage sensors using the linear unmixing approach of phasor FLIM

This alternative approach takes advantage of the linear unmixing capability of the FLIM phasor plot to resolve and quantify the fractional populations of distinct FRET states[21,22,46,47]. We consider the voltage sensor as existing in two conformational states: up and down states. The down-state model of the S4 corresponds to the low FRET state, while the up-state model corresponds to the high FRET state (Fig. 2a). In our tmFRET design, the low FRET state—arising when the donor–acceptor distance exceeds ~25 Å—results in minimal energy transfer, leaving the donor lifetime nearly identical to that of the donor

alone. As a result, the overall FRET signal is primarily determined by the efficiency of the high FRET state and the probability of the voltage sensor occupying that state.

To demonstrate linear unmixing in the phasor plot, we used cells expressing the hERG-L523TAG/G439TAA construct, dually labeled with Acd and Cu^{2+}-DOTA (Fig. 2b). Under depolarizing conditions achieved with 120 mM external KCl, the measured FRET can be resolved into two contributors: the donor only and the position of lifetime if 100% of the voltage sensors are in the high FRET state (Fig. 2b and Supplementary Fig. 3b). In a phasor plot, lines that connect different lifetime species are linear combination lines. The position of a phasor point along the line reflects the fractional contribution of each species in the mixture[46]. Here, linear fitting of the phasor data reveals a trend that follows the major axis of the elliptical cluster formed by membrane-localized pixels in the phasor plot. This axis likely reflects conformational heterogeneity among the channel population, with individual molecules adopting a range of S4 states. A more elongated major axis (i.e., a higher length-to-width ratio) may indicate greater variability in donor–acceptor distances across the channel ensemble. The measured high FRET value of 0.53, corresponding to a converted distance of approximately 13 Å, reflects the FRET efficiency of the high FRET state, and an estimation of the donor-acceptor distance in the up-state model. Based on the law of phasor additions[46], the fractional contributions of different lifetime species are inversely related to their distance from the composite phasor point in the plot—providing a quantitative basis for estimating the proportion of each state present. Therefore, the proportion of S4 segments in the high FRET state can be estimated by calculating the relative distances from the measured phasor position to the donor-only and high FRET reference points along the linear fit. As expected, membrane depolarization increased the proportion of the high-FRET state; approximately 35% of voltage sensors transitioned to the up state, consistent with the relatively low open probability of wild-type hERG channels at around +10 mV—a potential readily achieved by applying 120 mM extracellular KCl, as previously shown using voltage-sensitive dyes[38] (Fig. 2b). To establish a hyperpolarized baseline, we used extracellular NMDG to reduce resting membrane potential[48]. Further depolarization led to a greater fraction of the high-FRET state, with minimal changes in the amplitude of FRET efficiency (Fig. 2c). These results suggest that $hERG_{tmFRET}$ channels primarily occupy two discrete S4 conformations, with limited sampling of intermediate states.

To demonstrate the sensitivity of our phasor FLIM-tmFRET strategy in detecting small distance changes, we used a single mutation, D540K, which induces a "U-shaped" G-V relationship[49]. Notably, hERG-D540K channels exhibit pronounced hyperpolarization-activated currents reminiscent of pacemaker HCN channels, alongside depolarization-activated currents (Supplementary Fig. 4 a-d). The

D540K mutation disrupts a critical salt bridge between D540 at the C-terminal end of the S4 and R665 in the C-terminal end of the S6 helix (Supplementary Fig. 4 a). This disruption leads to the decoupling of the S4 and S6, resembling the structural arrangement observed in HCN channels, where the S4 presumably relies on coupling with the S5 helix rather than with the S6 helix for hyperpolarization-dependent activation[10,11,50]. To restore the wild-type behavior of the channel, we engineered a charge-swapping mutant, hERG-D540K/R665E (Supplementary Fig. 4 c-d), to recreate the salt bridge and thereby reestablish the S4-S6 coupling[49]. This intervention successfully rescued the native function of hERG channels.

The distinctive U-shaped G-V profile of the D540K mutation suggests the presence of multiple functional and conformational states of the S4 voltage sensor. To test whether these states correspond to distinct FRET efficiencies, we introduced the D540K mutation into $hERG_{tmFRET}$ channels. In the presence of D540K, phasor analysis revealed clear differences in tmFRET efficiency under hyperpolarized versus depolarized conditions (Supplementary Fig. 4e–f, Supplementary Fig. 5 a, c). In contrast, channels containing double D540K/R665E mutations exhibited only a single high-FRET state (Supplementary Fig. 5 b, c). These results suggest that D540K introduces distinct S4 conformations that likely contribute to the U-shaped gating behavior, while the R665E addition restores the all-or-none S4 transitions characteristic of the $hERG_{tmFRET}$ channel (Supplementary Fig. 5). This comparative analysis underscores the sensitivity of FLIM phasor analysis in detecting subtle distance changes between FRET pairs arising from voltage sensor rearrangements.

We also tested a tmFRET pair using the hERG L523TAG/A430TAA construct (Supplementary Fig. 6). In this case, even in the down state of S4, the proximity of the donor and acceptor resulted in noticeable FRET signals. As a result, the Acd lifetime distribution displayed a distinct arc shape, contrasting with the elliptical pattern observed in the hERG L523TAG/G439TAA construct. The primary lifetime distribution after a linear fitting, yielded a notably higher FRET efficiency (~60% efficiency), whereas the minor component of the lifetime distribution exhibited a lower FRET efficiency (Supplementary Fig. 6 b-d). The presence of this minor component complicated the accurate fitting of the lifetime distribution, especially when assessing the existence of additional intermediate FRET efficiencies, unless a second harmonic of the light modulation frequency was included[51,52]. Nevertheless, these results emphasize the ability of our FLIM-tmFRET strategy to reliably report S4 movement, with FLIM-tmFRET measurements showing dependence on both donor/acceptor proximity and voltage changes (Supplementary Fig. 6 e-f). Because linear unmixing analysis is most effective in systems that approximate a two-state model—especially when one state exhibits minimal FRET, as observed in the

L523/G439 FRET pair—we focused on the hERG L523/G439 pair ($hERG_{tmFRET}$ construct) for testing the LQTS mutations.

Phasor FLIM-tmFRET reveal intermediate FRET states of hERG voltage sensors caused by R531Q

Using the same L523/G439 pair in $hERG_{tmFRET}$, we tested the impact of the LQTS mutation R531Q on voltage sensor conformations (Fig. 3d). Our phasor analysis revealed at least two different FRET efficiencies: a lower one around 0.25 and a higher one similar to those observed in tmFRET experiments using the $hERG_{tmFRET}$ (Fig. 3 d-e). These findings suggest the presence of an intermediate conformation of the S4 voltage sensor induced by R531Q, exhibiting increased donor–acceptor distances (Fig. 3f). There was a notable prevalence of voltage sensors in the FRET state, even under more hyperpolarized voltages, with no increase upon voltage elevation in our experimental conditions (Fig. 3g). Given the pronounced right shift in the G-V curve of hERG-R531Q+ channels, a more depolarized voltage (> +60 mV) might be necessary to observe an increase in the percentage of the FRET state. At hyperpolarized voltages, the voltage sensor primarily transitions between the down and intermediate states relatively frequently (Fig. 3g, and percentage of FRET state = ~20%), while at more depolarized voltages, it can ascend to the up state. The donor-acceptor distance of 19 Å, derived from the measured intermediate FRET efficiency (in comparison to 13 Å for the high FRET state), aligns with the intermediate conformation of VSD predicted by the cryo-EM structure of Eag channels[12].

To further validate the robustness of our method and test the hypothesis that R531Q produces additional intermediate conformational states of S4, we designed alternative FRET pairs. Using the same FRET donor site, L523TAG, we selected two additional acceptor sites: T436, and P440 (Fig. 3a). Both constructs, paired with L523TAG, exhibited noticeable membrane-localized YFP expression after employing the dual stop-codon suppression strategy. Compared to the L523/G439 FRET pair, the L523/P440 pair demonstrated lower FLIM-tmFRET efficiency, whereas the L523/T436 pair exhibited higher efficiencies in the presence of 120 mM KCl (Fig. 3b). Overall, the converted distances for the four FRET pairs exhibited differences consistent with their respective positions in our structural models, despite potential variability introduced by donor–acceptor rotamer conformations inherent to this type of FRET measurement (Fig. 3c and Supplementary Fig. 7a). In addition, linear regression analysis revealed a strong negative correlation (coefficient r = -0.88) between the measured FRET efficiencies and the backbone-atom distances of these FRET pairs in hERG homology models with S4 in the up state. Regarding the L523/P440 pair, similar to the FRET changes observed with the L523/G439 pair, only a single high-FRET state was detected, with the percentage of this state adjustable by altering membrane

voltage using external NMDG or 120 mM KCl (demonstrated with the L523/P440 pair in Fig. 3e-g). Moreover, the results obtained with the L523/P440 FRET pair in the presence of R531Q further support our conclusion that the R531Q mutation induces intermediate conformational states of the S4 helix in hERG channels (Fig. 4d). The observation of intermediate FRET efficiencies under less depolarized membrane conditions (such as NMDG and PBS) aligns with the findings from the L523/G439 pair and reinforces the notion that R531Q leads to distinct voltage sensor conformations (Fig. 3e-g). Additionally, since the L523/T436 pair shared the same limitation as the previously mentioned L523/A430 pair, we opted not to test the effect of R531Q on potential intermediate FRET efficiencies for this pair.

One major advantage of our phasor linear unmixing FLIM-tmFRET method over traditional ensemble FRET is its ability to quantitatively estimate the fractional population of distinct FRET or conformational states[24,53]. Using this approach, we determined that approximately 35% of the S4 in $hERG_{tmFRET}$ channels adopt the high FRET state under high KCl conditions, compared to only 20% in the $hERG_{tmFRET}$-R531Q channels. We found a tetrameric model where at least three subunits must be activated for pore opening fitted our data best, compared to models requiring either one, two, or four subunits to be activated (see Methods and Supplementary Table 1). The corresponding Boltzmann free energy changes (ΔG) for tetramer activation of hERG were 1.1 kcal/mol for WT and 2.4 kcal/mol for R531Q. Notably, these estimates are close to ΔG values independently derived from patch-clamp G-V relationships, which yielded 1.3 kcal/mol (WT) and 2.9 kcal/mol (R531Q). This consistency highlights the effectiveness of our FLIM-tmFRET approach in extracting energetically meaningful parameters of conformational equilibria.

Collectively, these results indicate that: (1) the FLIM signals we measured predominantly originate from membrane-localized hERG channels; (2) dual stop-codon suppression enables the incorporation of Acd and ProK, yielding functional VSDs that respond to membrane potential changes; and (3) The phasor linear unmixing FLIM-tmFRET method provides accurate measurements of short-range distance changes between membrane helices in a near-native lipid environment, while simultaneously enabling quantification of conformational state populations and associated free-energy differences.

Molecular dynamics simulations suggest R531Q induces distinct conformations of the S4

We performed MD simulations to gain structural insights into the conformational dynamics and heterogeneity of the hERG VSD. When a hERG channel tetramer, modeled based on the cryo-EM structure of the Eag channel in the down conformation, was relaxed in a native lipid environment at -150

mV using molecular dynamics (MD) simulations[54], we observed that the S4 helix adopted the down conformation in two out of the four VSDs. In the other two VSDs, however, it adopted an intermediate conformation, similar to the intermediate-state cryo-EM structure of Eag-channel VSD and the intermediate I state inferred from tmFRET results (Supplementary Fig. 8), providing initial MD-based evidence of this intermediate state. When we repeated the simulations at -150 mV and 0 mV for a monomeric hERG transmembrane domain, the VSD was also stabilized in the intermediate I conformation (Fig. 4a). Previous studies have shown that the VSD of KCNH channels can function as a relatively independent unit[55,56]. This is exemplified in hERG and Eag channels, where split constructs with covalently disconnected VSDs and pore domains can reassemble into functional channels[55]. For Eag channels, even when both the entire N- and C-terminal regions are deleted, the channels still retain normal depolarization-dependent activation properties[56].

To evaluate how the R531Q mutation alters the resting conformation of the hERG VSD, we simulated the relaxed state of the mutant hERG VSDs at -150 mV in both monomeric and tetrameric configurations. Since FRET efficiencies differed at hyperpolarized voltages (NMDG and resting) but were mostly similar at depolarized voltages (high KCl) among various hERG mutations, we performed unbiased simulations of the relaxed VSD of the R531Q mutant at a hyperpolarized voltage (-150 mV) and in a lipid environment to identify potential structural differences compared to the WT (Fig. 4a). These simulations were also started using homology models of hERG based on the new cryo-EM structure of Eag channels with VSD in the down state[12]. To simplify the analysis, we modeled full-length hERG tetramers as well as hERG monomers including only the S1–S6 helices, incorporating R531Q. We found that in both models, the S4 helix in VSDs containing the R531Q mutation was elevated relative to the WT, stabilized in a position intermediate between the intermediate I and the S4-up conformations (Fig. 4a). Perhaps for the WT, the S4 may transition to the up position more readily, without encountering the energetic barrier that appears to trap R531Q in an intermediate state. This structural shift caused by R531Q is consistent with the reduced tmFRET efficiency and the corresponding FRET-predicted increase in donor–acceptor distances observed in the presence of R531Q (Fig. 4b and see details in Methods). Additionally, at hyperpolarized -150 mV, R531Q caused a nearly 30° tilt in the lower half of the S4 (Fig. 4a and Supplementary Fig. 9). R531Q also altered the secondary structure of the S4, switching it from a predominantly α-helical configuration in the WT to a more pronounced 3_{10}-helical conformation (Supplementary Fig. 9a, b).

To explore the dynamic pathway of the S4 movement and its alteration by the R531Q mutation, we performed nonequilibrium MD simulations, specifically steered MD (SMD). The 100 ns SMD started

from the intermediate conformation I to the up-state conformation of the S4, in a monomer transmembrane domain (S1-S6 helices) under 0 mV (Fig. 4c, e-g, and Supplementary Movie 1). As an SMD reference, we used the central positions of the K525, R528, and R531 side chains relative to the S2 helix as collective variables[57-59]. The S4 showed the expected upward displacement of the S4, adopting a new intermediate conformation, termed intermediate II, likely driven by competition between R528 and K525 for interaction with D456 in the S2 helix (Fig. 4c, e-g). The S4-up position was subsequently stabilized by the interaction between R531 and D460 in the S2 helix. In this context, R531 promotes S4 upward movement, while K525 (K1) acts as an impediment, helping to explain why the LQTS-associated K525N mutation enhances hERG channel sensitivity to depolarizing voltages[25,60]. Overall, the S4 helix exhibited a modest displacement, with a 5 Å shift in the R531 side chain (Fig. 4f) and a 3 Å shift in the backbone of its N-terminal region (Fig. 4g), primarily reflecting the movement of R531 from below to above F463 in the charge transfer center. The modest scale of S4 movement is consistent with the relatively shallow G-V relationship of hERG channel activation. Note that the full range of S4 displacement is likely greater, as our SMD simulations begin from the intermediate I state rather than the fully down state.

In SMD simulations of the R531Q mutant, the S4 helix began in a more elevated position, resulting in subtler displacement during the first half of the simulation (Fig. 4d, e-g, and Supplementary Movie 2). No distinct intermediate dwell states were observed between the initial (intermediate I) and up conformations. These altered dynamics in the R531Q mutant likely contribute to its impaired voltage-sensor activation observed in functional studies.

R528Q mutation promotes similar FRET intermediates and S4 rearrangement

To further elucidate the mechanisms by which arginine mutations impact S4 helix movement, we tested the presence of intermediate FRET states in hERG channels containing the R528Q mutation using the same tmFRET design. The R528P mutation is a novel mutation associated with LQTS[27]. However, because proline is a helix-breaking residue and may cause protein misfolding, we did not include the R528P in this study.

As mentioned earlier, R528Q mutation induced biphasic channel activation, yet did not significantly alter the G-V relationship compared to WT+ channels (Supplementary Fig. 1d). Similar to the tmFRET results of R531Q mutant channels, phasor analysis revealed the presence of at least two different FRET efficiencies: a lower one around 0.35 (a converted distance of 16.6 Å) and a higher one

around 0.5 (Fig. 5 a-d), suggesting that the intermediate state of S4 with R528Q likely resides in a similarly more elevated position as in the R531Q mutant, and is thus designated as intermediate state II. Notably, unlike the R531Q mutant channels (as depicted in Fig. 2g, Fig. 3g compared with Fig. 5d), membrane depolarization increased the proportion of FRET states for R528Q-containing channels, indicating a higher probability of the S4 helix in the intermediate II or the up states. This observation contrasts with the behavior observed in R531Q channels and is consistent with the relatively unaffected $V_{1/2}$ in the G-V relationship of R528Q channels (Supplementary Fig. 1d).

In MD simulations of the hERG VSD containing the R528Q mutation, we observed a similar elevation and tilt of the S4 segment at the resting hyperpolarized voltage (-150 mV) (Fig. 5 e-h and Supplementary Fig. 9). The S4 tilting, measured at 34°, occurs near the Q528 site, in contrast to the R531Q mutant, where the tilt is closer to the Q531 site (Supplementary Fig. 9c, e). R528Q produced a similar effect in promoting the 3_{10}-helical conformation in this resting state. SMD simulations of the R528Q mutant suggest that prolonged dwell time in the elevated S4 position may underlie the intermediate FRET observed (Fig. 5 e-h, and Supplementary Movie 3). Overall, S4 movement is less disrupted by the R528Q mutation than by R531Q, consistent with the markedly greater functional impact of R531Q compared to R528Q or other S4-arginine neutralizations.

Additionally, we performed analogous equilibrium MD simulations of the R534Q and K525N mutants at -150 mV. These charge-neutralizing mutations also induced minor tilting of the S4, though the structural changes caused by R534Q and K525N were considerably less pronounced compared to those in R528Q and R531Q mutants (Supplementary Fig. 9). To assess functional consequences, we carried out parallel tmFRET experiments on $hERG_{tmFRET}$ channels including the LQTS-associated R534Q mutation (Supplementary Fig. 10). These experiments revealed a single high FRET state, distinct from the profiles of R528Q and R531Q mutants, but similar to $hERG_{tmFRET}$ channels, suggesting a different disease-causing mechanism that affects S4 movement. R534 is in the lower portion of the S4 helix and may reside outside or only partially within the transmembrane electric field during voltage sensing. The inactivation of R534L (and R534Q) at more depolarized voltages may instead underlie its contribution to LQTS (Supplementary Fig. 1e). Furthermore, analogous experiments using $hERG_{tmFRET}$ channels with the K525N mutation revealed also a single high-FRET state, but with a substantially higher FRET efficiency of 62 ± 0.5% (n = 12 cells). This result is consistent with the idea that the S4 can move up further when the hindrance of K525 is abolished, which facilitates channel opening[25,60].

Free energy landscape of hERG voltage sensor dynamics

Dwells and pauses in the S4 displacement time course during SMD simulations suggest the presence of intermediate conformational states. To further assess the stability and energetic profiles of these putative metastable intermediates, we performed umbrella sampling simulations (Fig. 6)[57,58]. In this approach, multiple simulations were conducted with the system restrained at defined values of collective variables (CVs), referred to as windows along a reaction coordinate describing relative displacement of S4, without external voltage (0 mV). One-dimensional potentials of mean force (PMFs) were then calculated for the WT, R531Q, and R528Q VSDs. PMFs along the reaction coordinate were derived by reconstructing free energy profiles across all windows using the generalized weighted histogram analysis method (GWHAM)[61]. This analysis provided detailed energetic insights into how specific mutations reshape the conformational landscape of the S4. For the WT VSD, the PMF revealed at least two distinct free energy minima, corresponding to intermediate I and the up state (Fig. 6a). Importantly, in the WT free energy landscape, the final step appears to confer a kinetic barrier that hinders reversal (Fig. 6a). Furthermore, the R531Q and R528Q mutants also exhibited noticeable free energy minima corresponding to the SMD-observed dwells, indicating these as stable intermediate states (Fig. 6 b-c). In contrast to the WT, the R531Q mutant exhibits a smoother energy landscape with less barriers, allowing the S4 to transition more freely, including reversals to the more stable intermediate I state. This suggests a less stabilized up state (Fig. 6b). The R528Q mutant, by comparison, displays a free energy profile with multiple stable intermediates, including a lowest-energy intermediate II state (Fig. 6c). This altered energy landscape may underlie the characteristic slow deactivation, multiexponential activation kinetics, as well as the observed intermediate II FRET state of the R528Q mutant.

Together, our findings suggest that mutating key voltage-sensing arginines in hERG channels stabilize intermediate conformational states of the S4 helix. These intermediates provide a structural framework for interpreting and comparing to analogous states identified in other voltage sensors[12,62-64]. Integration of electrophysiology, FLIM-tmFRET, and MD simulations provides a comprehensive understanding of the mechanisms by which LQTS-associated mutations impair voltage sensing in hERG channels.

DISCUSSION

Currently, effective methods for probing the conformational dynamics and heterogeneity of membrane proteins in living cells are limited. While single-molecule FRET techniques offer substantial advantage in dissecting protein conformational states, their application in studying rapid and voltage-dependent events within native membranes remains challenging. Similarly, obstacles persist in employing methods such as cryo-EM and double electron-electron resonance (DEER), both of which routinely require cryogenic sample freezing. Fluorescence lifetime decays, like DEER signal decays, contain information that can be analyzed through multi-exponential functions, potentially unraveling distinct populations of fluorophores. Notably, these fluorescence lifetime techniques can be executed within native membranes and integrated with functional approaches like patch clamp. Leveraging a combination of genetic-code expansion, click chemistry, frequency-domain phasor FLIM, and tmFRET, we engineered a live-cell system to measure intermediate states of ion channel voltage sensors in a relatively high-throughput manner. While the phasor FLIM technique has been used in quantifying multiple states of FRET in the field of cell biology[22], its potential in elucidating the structural biology of proteins is only beginning to be realized[23,53]. This technique can be broadly applied to study protein dynamics, particularly for membrane proteins.

Building upon our findings, we postulate that neutralization of S4 positive charges in the charge transfer center (R2 and R3) gives rise to distinctive intermediate states within the S4 helix voltage sensor (Fig. 6d). Specifically, the negatively charged residues situated within the S2 and S3 helices, known as the extracellular negative cluster (ENC; D456 and D460) and intracellular negative cluster (INC; D411, D466 and D501), play a role in stabilizing these intermediate states. In the case of R531Q mutation, the positively charged side chain of R528 is essential for S4 to interact with the ENC, thereby stabilizing its intermediate state. In contrast, in the instance of the R528Q mutation, S4 depends on the positive charge of the lower R531 to interact with the ENC, thereby resulting in a slightly upward shift of S4, compared to that for the R531Q mutation (Fig. 6d). In other words, as the S4 moves upward, the intermediate states get stabilized when neutralized arginine side chains fail to exchange their ion pair partners[64]. Interestingly, the contrasting activation patterns observed between R531Q channels (long initial lag and mono-exponential activation) versus R528Q channels (short initial lag and double-exponential activation) may be due to the distinctive functional coupling of the intermediate II S4 conformation to channel opening. Stabilizing the intermediate II conformation may hinder pore closure, as evidenced by the significantly slower deactivation observed in the R528Q mutant, which has a low-energy intermediate II state in its free energy landscape (Fig. 6c). Conversely, stabilizing the intermediate I conformation in R531Q could

prevent pore opening (Fig. 6b). Furthermore, disrupting the characteristic "RXX" repeat can split the movement of the voltage sensor into distinct phases, a behavior reminiscent of the biphasic S4 movement observed in the VSD of various other proteins and channels[63,65-67]. Finally, our results provide insights to analogous S4-arginine (R2 and R3 positions, Supplementary Fig 1) mutations that cause cardiac diseases in other types of VGICs, e.g., in voltage-gated Na^+ channels[68-71].

Our MD simulations provide new insights into S4 movement in VGICs, particularly those in non-domain-swapped subunit arrangements, such as KCNH family channels[72,73]. They built upon newly available structural data of the Eag channel in the S4 down-state (cryo-EM)[12], and employed extended, structurally guided protocols that enable more accurate modeling of S4 conformations at hyperpolarized voltages and the dynamic movement of S4—an advance over earlier methods[74]. The elevated S4 helix position induced by arginine mutations aligns with intermediate states predicted by FRET experiments. While some S4 arginine mutations generate gating pore currents in VGICs[75,76], R531Q produced little ionic current at hyperpolarized voltages. In non-domain-swapped VGICs, the closer spatial proximity of S4 to S5 raises the possibility that arginine mutations may influence the pore domain through distinct mechanisms compared to domain-swapped VGICs[9,11,12,73]. Future studies should explore how these structural rearrangements induced by mutations modulate VSD-PD coupling within the context of tetrameric channels. Additionally, it remains unclear whether a potential 3_{10}-helix to α-helix conversion modulates the intermediate state of voltage sensors[12,16,25,77,78]. In our SMD (Supplementary Movies 1-3), we noticed that during the upward movement of S4, S4 regions transitioned from an α-helical to a 3_{10}-helical conformation while traversing the charge transfer center. This possible rearrangement allows the voltage-sensing arginines to align on one side of the helix with minimal rotation of S4[12]. The observation that arginine mutations promote a 3_{10}-helical conformation at the resting S4 (intermediate I) state suggests that such structural alterations could contribute to the functional changes, potentially by affecting the stability, movement, or energetics of the S4 in VGICs. Moreover, the tilt of the S4 caused by arginine mutations is reminiscent of similar motions observed in the S4 of non-domain-swapped VGICs, particularly in HCN channels[10,18,50,79]. This suggests that the C-terminal half of the S4 segment in this VGIC configuration is highly susceptible to tilting or bending motions, which plays a significant role in shaping the diversity of voltage-dependent gating mechanisms in KCNH channels.

Our method represents a significant technical advance in the application of FLIM-FRET to structural biology in live-cell imaging experiments and shows promise for future improvement. Enhancing the selectivity of pyrrolysyl-tRNA synthetase for Acd is essential to minimize nonspecific fluorescence. The presence of endogenous genes using the amber codon might interfere with the Acd system, resulting

in undesired cytosolic Acd fluorescence in our preparations. Developing an Acd variant that fluoresces exclusively upon incorporation into the protein of interest would help mitigate the nonspecific Acd fluorescence as well. Furthermore, the inherent flexibility of the extended linker length of the ProK-Azide-DOTA remain limiting factors for precise absolute distance measurements. Optimizing the linker length between ProK and azido DOTA could bring the transition metal acceptor closer to the protein backbone. This engineering can also benefit from more efficient CuAAC click chemistry, requiring lower concentrations of Cu(I) catalyst and exhibiting faster reaction kinetics. Alternatively, engineering copper-free strain-promoted azide-alkyne cycloaddition (SPAAC) reactions could also facilitate labeling of the tmFRET acceptor[80,81]. Such improvements would not only enhance the accuracy of this method but also reduce the cytotoxicity associated with transition metals. Finally, incorporating patch clamp techniques into this method to precisely control membrane voltage could further enhance our ability to correlate channel function with structural states.

MATERIALS AND METHODS

Molecular Cloning

Bioorthogonal labeling of noncanonical amino acids (ncAAs) was achieved by site-specific incorporation using either single or dual codon suppression. This involved using amber (TAG) and ochre (TAA) codons within the channel protein of interest, specifically the hERG1 cDNAs synthesized by VectorBuilder (Chicago, IL). These constructs, featuring a C-terminal eYFP and a CMV promoter, were cloned and amplified using a mammalian gene expression vector. The S620T mutation, located in the pore helix of the channel, was included in all hERG1 constructs used in this study to eliminate rapid C-type inactivation[30-32]. This modification allows for a more accurate estimation of voltage-dependent activation by avoiding the overlap between activation and inactivation phases. Moreover, we believe that the S620T mutation does not impact the structure and function of the VSD. For simplicity, we refer to the modified hERG1-S620T-YFP channel as the "WT+" channel, and the hERG1-L523TAG/G439TAA, S620T-YFP as "$hERG_{tmFRET}$" throughout this paper.

DNA oligo primers, from Integrated DNA Technologies (IDT, Coralville, IA), were used for the design and synthesis process. Point mutations were induced using either the QuikChange II XL Site-Directed Mutagenesis or Multi Site-Directed Mutagenesis Kit (Agilent Technologies, Cedar Creek, TX). Subsequently, Dpn I restriction enzyme treatment (Agilent Technologies) was applied to digest the methylated parental DNA template of the DNA plasmids, which were then transformed into XL10-Gold competent cells (Agilent Technologies). The introduction of double functional stop codons opal (TGATGA) at the terminal end of YFP ensured successful translation termination. Verification of the introduced stop codons within the mutant plasmid was performed through DNA sequencing provided by either Genewiz (Azenta Life Sciences, Burlington, MA) or Plasmidsaurus (Eugene, OR). Additionally, the DNA concentration was quantified using a Nanodrop OneC spectrophotometer (Life Technologies, Grand Island, NY).

Cell Culture, Transient Transfection and Bioorthogonal Labeling

The tsA-201 cells, a variant of human embryonic kidney (HEK293) cells, were procured from Sigma-Aldrich (St. Louis, MO), authenticated via short tandem repeat (STR) profiling, and then cryopreserved in liquid nitrogen. For initiating new cell cultures, these cells were thawed and cultured in Dulbecco's modified Eagle's medium (DMEM; Gibco), supplemented with 10% fetal bovine serum (FBS;

Gibco) and 1% penicillin/streptomycin (Gibco), within a humidified incubator maintained at 37 °C with 5% CO_2.

Transfection was performed on 70% - 90% confluent tsA-201 cells using the lipofectamine 3000 kit (Invitrogen, Carlsbad, CA, #L30000080), following established protocols[82,83]. For dual stop-codon suppression, the cells were co-transfected with two plasmids: pAS_4xU6-PylT M15(UUA) FLAG-Mma PylRS (Mma PylT/RS) from Addgene (Watertown, MA, #154774)[41] and the Acd RS1 tRNA/aminoacyl-tRNA synthetase pair (GCE4All Research Center, Oregon State University, and Addgene #197566)[40], along with a third plasmid containing the dual stop-codon mutations (TAG and TAA) of the hERG gene required for selective incorporation of two noncanonical amino acids (ncAAs): Acd (the Petersson Lab, University of Pennsylvania) and N-propargyl-L-lysine (ProK) (SiChem, Bremen, Germany)[41]. This Acd RS1 tRNA/aminoacyl-tRNA synthetase pair consists of one copy of aminoacyl-tRNA synthetase and four copies of tRNA. To facilitate nonsense suppression, a human dominant-negative release factor eRF1 (E55D) (VectorBuilder, Chicago, IL) was co-transfected[84]. The ncAAs were added to the transfection solution: 5 μM Acd and 0.25 mM ProK. ProK was mixed with 1 M HEPES solution in a 1:4 ratio (Sigma-Aldrich, St. Louis, MO) before adding to cell culture. The ProK stock solution (100 mM) were made by dissolving ProK in 0.2 M NaOH water. In the absence of the pAS_4xU6-PylT M15(UUA) FLAG-Mma PylRS (Mma PylT/RS) while in the presence of the Acd incorporation system, we did not observe significant membrane-localized YFP signals (Supplementary Fig. 2f), indicating the Acd RS1 tRNA/aminoacyl-tRNA synthetase pair is specific to the amber stop codon and cannot suppress the ochre stop codon. In addition, we conducted experiments expressing $hERG_{tmFRET}$ constructs with aminoacyl-tRNA synthetases but without Acd and ProK amino acids and observed no detectable currents—similar to untransfected cells—in the presence of 10 mM TEA in the bath solution.

At the ProK site, we conducted the copper-catalyzed azide-alkyne cycloaddition (CuAAC) reaction using 50 μM $CuSO_4$, 250 μM THPTA (Tris(benzyltriazolylmethyl)amine), and 2.5 mM ascorbic acid in DMEM medium[41]. For azido-DOTA labeling (at 100 μM in cell culture), the incubation proceeded for 1-1.5 hours at 37 °C. To produce Cu^{2+}-DOTA, we mixed equal amounts of 100 mM azide DOTA stock and 110 mM $CuSO_4$ stock, allowing them to incubate for five minutes until the mixture transitioned from light to darker blue, indicating Cu^{2+} binding to DOTA. Once bound, DOTA and Cu^{2+} dissociation occurred very slowly due to their picomolar affinity[38]. The azido-mono-amide-DOTA was purchased from Macrocyclics, Inc (Plano, TX). We tested different durations for the azido-Cu^{2+}-DOTA labeling (30 mins, 1 hour, and 1.5 hours) to assess completeness and found that the Acd lifetime shift plateaued around 1-1.5 hours, which is consistent with the relative fast kinetics for this type of click chemistry[80]. For certain acceptor sites such

as A430, which is more membrane-embedded, slightly longer labeling times may be required to achieve full labeling efficiency. However, azido-Cu^{2+}-DOTA labeling beyond 2 hours caused noticeable cytotoxicity; therefore, labeling duration was restricted to a maximum of 2 hours.

Fluorescence Microscopy, Fluorescence Lifetime measurement and FLIM-FRET

Fluorescence measurements were conducted using an Olympus IX73 inverted microscope (Olympus America, Waltham, MA), equipped with a 60× U Plan S-Apo 1.2-NA water-immersion objective. Epifluorescence recording was facilitated by wide-field excitation from a pE-800 LED light source (CoolLED, Andover, UK). For choosing cells with strong membrane localized YFP fluorescence via eyepiece of the microscope, YFP was excited using a 500 nm LED line. Acd fluorescence was expected in these cells and was excited using a 365 nm LED line. The imaging solution used for cell visualization was Dulbecco's phosphate-buffered saline (PBS, ThermoFisher), unless specified otherwise. All microscopic experiments were conducted at room temperature.

Spectral measurements of Acd fluorescence used a spectrograph (SpectroPro 2156, 300 groves/mm grating, 500 nm blaze; Teledyne Princeton Instruments, Acton, MA) situated between the microscope output port and an INFINITY3S-1URM CCD camera (Teledyne Lumenera, Ottawa, ON). Acd fluorescence from cells was excited using a 365 nm LED line through a filter cube. The emission filter was removed from the filter cube, allowing only fluorescence in the wavelength range of 423 to 597 nm collected as a spectral image. Spectral images were acquired with exposure times of 500 ms. In addition, spectral measurements of the light absorption of transition metals were made using the Nanodrop OneC spectrophotometer (Life Technologies, Grand Island, NY). Subsequent analysis of the spectral data was conducted using ImageJ/Fiji (National Institutes of Health, USA) and Igor Pro 9 (Wavemetrics, Portland, OR).

Digital frequency-domain fluorescence lifetime imaging was conducted using a Q2 laser scanning confocal system, which was equipped with a FastFLIM data acquisition module (ISS, Inc, Champaign, IL) and two hybrid PMT detectors (Model R10467-40, Hamamatsu USA, Bridgewater, NJ), as previously described[21,38,85]. This confocal FLIM system is integrated with the Olympus IX73 inverted microscope. The fluorescence lifetime measurements encompass both frequency-domain (allowing instantaneous distortion-free phasor plotting) and time-domain decay information. To excite Acd, a 375 nm modulated diode laser (ISS, Inc) controlled by FastFLIM was used, with the emitted fluorescence captured through a 447/60 nm band-pass emission filter. YFP excitation was achieved using a 488 nm wavelength

excitation and collected through a 542/27 nm emission filter. Simultaneous two-color imaging was facilitated by dichroic cubes, with one containing a 50/50 beam splitter and the other equipped with long-pass filters.

For image acquisition, confocal images with a frame size of 256 x 256 pixels were obtained for each experimental condition, using a motorized variable pinhole (set at a size of 100 μm). To determine the phase delays (φ) and modulation ratios (m) of the fluorescence signal in response to an oscillatory stimulus (6 ps per pulse) with a frequency ω = 20 MHz, the VistaVision software (ISS, Inc) associated with the FastFLIM system was used. These values were obtained by performing sine and cosine Fourier transforms of the phase histogram, taking into account the instrument response function (IRF) calibrated with Atto 425 in water (with a lifetime of 3.6 ns, see Supplementary Fig. 2). VistaVision software, equipped with the imaging and FLIM module, was also used for image processing, display, and acquisition. This software allowed for the specification of parameters such as pixel dwell time, region of interest, and resolution. Additionally, it employed a fitting algorithm, phasor linear unmixing analysis for FLIM-tmFRET analysis. To enhance display and analysis of membrane-localized lifetime species, a median/gaussian smoothing filter and an intensity-based selection of the membrane region were applied. The VistaVision and phasor FLIM provide a significant advantage by effectively differentiating signals originating from background and cytosolic fluorescence outside the membrane region from those within the plasma membrane. This capability is especially important given that our Acd incorporation system tends to generate substantial nonspecific cytosolic Acd fluorescence, which constitutes the primary error source in our experiments. Relying on the selection of cells exhibiting strong membrane-localized YFP fluorescence enabled us to analyze lifetime species of the Acd fluorescence mostly aligned with YFP fluorescence associated the plasma membrane (Supplementary Fig. 2). The exact reason for the greater cytosolic Acd fluorescence comparing to other systems that incorporate fluorescent noncanonical amino acids (e.g. L-Anap) via stop-codon suppression is unclear[38,40,45,86], and likely due to the high membrane permeability of Acd, potential high affinity between Acd and its tRNA, and nonspecific amber stop-codon suppression of endogenous genes. Additionally, we engineered a similar plasmid containing the Acd RS1 tRNA/aminoacyl-tRNA synthetase pair with one copy of aminoacyl-tRNA synthetase but only two copies of tRNA, which was sufficient to achieve dual-stop-codon suppression, indicated by significant membrane-localized YFP fluorescence. However, this modification did not reduce the nonspecific cytosolic Acd fluorescence.

The VistaVision software features the FRET trajectory function to estimate the FRET efficiency, manifesting an averaged distance between donor and acceptor probes. As previously described, key

parameters are adjusted to optimize the fitting trajectory through both the donor alone and the donor species due to quenching by FRET acceptors[38]. Regarding the linear unmixing (decomposition) approach of calculating FRET efficiency, the linear fitting process underwent visual inspection to derive four parameters: (1) background contribution in the donor-alone (or low FRET) sample, (2) background contribution in the donor sample in the presence of the acceptor, (3) percentage contribution by the FRET state, and (4) FRET efficiency under theoretical conditions where 100% donors undergo high FRET. Background fluorescence remained within the cytosol and the levels typically at or below 5%, consistent with the minimal emission intensity observed in untransfected cells. To determine the percentage contribution by the FRET state, the cursor position was adjusted to cover the central portion of the lifetime distribution. The FRET efficiency of the low FRET state corresponding to the down state of the S4 cannot be accurately measured since the lifetime species typically would not exhibit an elliptical distribution and localize very close to the donor alone phasor.

The distances *r* between the Acd and Cu^{2+}-DOTA acceptors were estimated using the convolution of the Förster equation ($E_{max.} = 1 / (1 + (r / R_0)^6)$) with a Gaussian function: Förster convolved Gaussian (FCG) as previously established[10,86]. The FCG adopts a Gaussian distribution with a standard deviation (σ) of 7.5 Å and a full width at half maximum (FWHM) of 17.7 Å (Supplementary Fig. 5). This assumption was based on the interatomic distance distribution of probes with similar labels, e.g., the L-Anap and Cu^{2+}-TETAC tmFRET pair[10,24,86]. The R_0 value was calculated using the following equation:

$$R_0 = C\sqrt[6]{JQ\eta^{-4}\kappa^2} \qquad (1)$$

where C is the scaling factor, J is the overlap integral of the Anap emission spectrum and the YFP absorption spectrum, Q is the quantum yield of the Acd (~0.8), η is the index of refraction, and κ^2 is the orientation factor. η was assumed to be 1.33, and κ^2 was assumed to be 2/3. This calculation generated a R_0 of 13 Å between Acd and Cu^{2+}-DOTA and 12 Å between Acd and Co^{2+}-DOTA.

To assess the effectiveness of the FCG-based distance estimation, we compared the distances estimated by tmFRET for the L523/G439 and L523/P440 FRET pairs to the corresponding Cβ(L523)–Cα(G439 or P440) distances from MD simulations of the R531Q VSD at hyperpolarized voltages and the WT VSD in the up state (Fig. 4b). While the absolute distances predicted by tmFRET were about 5 Å different from the Cβ–Cα distances—likely due to the linker lengths and side-chain positions of the FRET donors and acceptors—the change in distance (ΔD) from the intermediate state of R531Q to the up state closely agreed between the two approaches. For the L523/G439 pair, the ΔD was 5 Å from tmFRET and

4 Å from MD simulations; for the L523/P440 pair, the ΔD was 3 Å and 4 Å, respectively (Fig. 4b). These findings underscore the accuracy of our phasor FLIM-tmFRET method in predicting conformational changes within the VSD.

Patch-Clamp Electrophysiology

Whole-cell patch-clamp recordings were conducted at a temperature range of 22 - 24 °C using an EPC10 patch-clamp amplifier and PATCHMASTER (HEKA) software. Borosilicate patch electrodes, with an initial pipette resistance of approximately 3 - 5 MΩ, were fabricated using a P1000 micropipette puller from Sutter Instrument (Sutter, Novato, CA). Current signals were low-pass filtered and sampled at a frequency of 10 or 5 kHz. Series resistance was mostly under 10 MΩ and compensated at ~ 40-70%. Patch clamp was performed using a Sutter MP-225A motorized micromanipulator (Sutter, Novato, CA).

To record hERG currents from tsA-201 cells, the internal pipette solution was prepared with the following composition (in mM): 10 NaCl, 130 KCl, 3 $MgCl_2$, 10 HEPES, 0.5 EGTA, 1 MgATP, 0.3 Na_3GTP, and pH 7.2 adjusted with KOH. The external solution used was Ringer's solution with the following composition (in mM): 160 NaCl, 2.5 KCl, 1 $MgCl_2$, 2 $CaCl_2$, 10 HEPES, 8 D-Glucose, and pH 7.4 adjusted with NaOH. 10 mM TEA was added to the external solution to block endogenous potassium currents of tsA cells, while having minor effect on the hERG currents[29]. For hyperpolarizing and depolarizing solutions, 107 mM impermeant cation NMDG (N-methyl-D-glucamine) and 120 mM KCl replaced NaCl in the Ringer's solution, respectively[48].

The conductance-voltage (G-V) relationships were determined by analyzing the instantaneous tail currents subsequent to voltage pulse steps. Subtraction of leak tail currents was performed, and the resulting currents were normalized to the maximum tail current amplitude (G/G_{max}). The relative conductance was then plotted against the voltage of the main pulse and fitted using the Boltzmann equation:

$$G/G_{max} = 1/(1 + \exp[(V_{1/2} - V)/V_s]) \qquad (2)$$

where V is the membrane potential, $V_{1/2}$ is the potential for half-maximal activation, and V_s is the slope factor. The difference in free energy between the channel closed state and open state at 0 mV was calculated according to: $\Delta G = RTV_{1/2}/V_s$, where R is universal gas constant and T is room temperature in

kelvin (297 K). A more positive ΔG value indicates a greater energetic favorability for the channel to remain closed at 0 mV.

As a comparison, to calculate the Boltzmann free energy difference (ΔG) between the channel opening and closing at the high KCl condition in our FRET experiments, given the fraction of S4 in the activated high-FRET state, we used the following equation derived from the Boltzmann distribution:

$$\Delta G = -RT\ln((P_{FRET})^n / (1 - P_{FRET})^n) \quad (3)$$

where P_{FRET} is the fraction of voltage sensors in the high FRET state. This expression assumes a tetrameric model, in which at least n of the 4 independent subunits need to be in the high FRET (activated) state for the channel to be considered open. We estimated the channel open probability (P_{open}) from P_{FRET} using the following binomial equation:

$$P_{open} = \sum_{k=3}^{4} \binom{4}{k} (P_{FRET})^k (1 - P_{FRET})^{4-k} \quad (4)$$

For $hERG_{tmFRET}$, when P_{FRET} is 0.35, the estimated P_{open}, calculated as the sum of binomial probabilities for at least three subunits being active, is about 13%. In contrast, for the hERG R531Q mutant with a P_{FRET} of 0.2, the estimated open probability drops to just 2.7%. Estimates using this "3-subunit" model align with the moderate activation of WT channels and the minimal or absent activation of the R531Q mutant near 0 mV—a voltage approximately achieved by extracellular 120 mM KCl in tsA cells[38] (Supplementary Table 1). Neither the "1-subunit" nor the "4-subunit" model produces channel opening profiles that align well with experimental observations (Supplementary Table 1). The "2-subunit" model, while closer, is likely unrealistic, as hERG channels probably do not reach 100% open probability even at saturating depolarizing voltages.

Modeling hERG VSD structures

Our initial hERG-VSD down-state model was constructed through homology modeling, using the cryo-EM structure of the VSD in the down state of an Eag channel (PDB: 8EP1) as a template[12]. To model the up-state conformation of the hERG voltage-sensing domain (VSD), we compared the cryo-EM structure of hERG (PDB: 5VA1)[14], a homology model based on the up-state VSD of the Eag channel (PDB: 8EOW), and an AlphaFold-predicted model[87]. All three models exhibited strong overall structural similarity. The S1-S2 loop region—where our FRET acceptor sites are located—is unresolved in cryo-EM

structures of hERG[14], and was further modeled using AlphaFold to estimate donor-acceptor distances for FRET analysis.

The down-state homology model was embedded in a lipid bilayer mimicking the sarcolemma, composed of phosphatidylcholine (PC, 33%), phosphatidylserine (PS, 3.5%), phosphatidylethanolamine (PE, 17%), phosphatidylinositol 4,5-bisphosphate (PI(4,5)P_2, 3.5%), cholesterol (33%), and sphingomyelin (10%)[88]. The system was built using CHARMM-GUI Membrane Builder and solvated in 0.15 M KCl using the TIP3P water model within a 205 Å x 205 Å x 190 Å unit cell[89]; the final assembly consists of 720k atoms. After equilibration, the WT tetramer system was simulated under an applied potential of -150 mV for 1 μs.

All MD simulations in this study were conducted using NAMD3 with a 2 fs timestep[90,91]. The systems were equilibrated under the NPT ensemble, maintaining the temperature at 310 K with the Langevin thermostat[92]. The Nosé–Hoover Langevin piston method was used to keep the pressure at 1 bar, and τ_p = 0.1 ps for 50 ns[93,94]. The protonation states for amino acid residues are as follows: Arg and Lys were protonated, Asp and Glu were deprotonated, and His had single protonation in their side chains. Particle mesh Ewald (PME)[95] summation was used for long-range electrostatic interactions, with a 12 Å cutoff, and a 10 Å switching distance was applied for van der Waals interactions.

The simulations were carried out with the CHARMM force field. Each system underwent CHARMM-GUI's standard multi-step equilibration protocol, during which positional restraints were gradually released over 2 ns prior to production runs. Point mutations were generated using the VMD Mutator Plugin. For the WT, R531Q, and R528Q systems, two or three independent replicas were performed. Convergence was evaluated by tracking RMSD of backbone atoms across trajectories (Supplementary Fig. 11), with all systems demonstrating stable behavior consistent with convergence by the end of the simulations.

Steered Molecular Dynamics (SMD) Simulations

For SMD simulations, a transmembrane domain (TMD), residues 405 - 667, of a monomer from hERG down state was embedded in a membrane, with the same composition as the equilibrium simulations described above and solvated in 0.15 M KCl using TIP3P water; the resulting system size was 150 Å x 150 Å x 130 Å; the total system size was 255k atoms. MD simulations of the TMD are computationally efficient, making them a practical choice for SMD simulations. This TMD was initially

simulated under the applied voltage of -150 mV to obtain a relaxed starting model, resembling the intermediate I state. SMD was then used to steer it to the VSD up state at 0 mV using three “distance Z” collective variables; the three collective variables were defined as the vertical displacement from the center of mass (COM) of K525, R528, and R531 sidechain atoms, with respect to the COM for the S2 helix backbone atoms. The target value for these variables was defined with respect to the structure of hERG, in the VSD up state captured by cryo-EM (PDB: 5VA1)[14]. Specifically, for SMD of the WT TMD, the distance values were 7.6 Å for K525, 3.0 Å for R528, -5.4 Å for R531 in the starting model, to 11.4 Å for K525, 6.3 Å for R528, and 0.9 Å for R531 in the up state. The S1-S3 helices were restrained with 10 kcal/mol/Å^2 harmonic restraints. For the SMD of R531Q and R528Q mutants, same collective variables for the up (end) state were used. Simultaneously, a pulling force was applied to each collective variable using a harmonic potential with a spring constant of 90 kcal/mol/Å^2. The SMD simulation was performed over 100 ns.

Umbrella Sampling Analysis of hERG S4 Movement

To quantify the free energy landscape associated with vertical translation of the S4 helix in the hERG VSD, we performed umbrella sampling simulations based on the SMD of WT, R528Q, R531Q VSDs[96]. The averaged center-of-mass (COM) z-coordinate of K525, R528 (or Q528) and R531 (or Q531) relative to the COM of S2 helix was chosen as the reaction coordinate, representing vertical displacement perpendicular to the membrane plane. The sampling range for each system was derived from its respective SMD trajectory. Twelve umbrella windows were constructed to evenly span the reaction coordinate. Initial configurations for each window were extracted from the corresponding SMD trajectories. Window spacing was ~0.35 Å for WT and R528Q, and ~0.25 Å for R531Q, adequately covering the expected conformational transition between the initial and up state. Each umbrella window was energy minimized and equilibrated for 22 ns, followed by a 10 ns production run under the NPT ensemble using NAMD3 with a 2 fs timestep. A harmonic restraint was applied to a collective variable defined as the distance between the average COM of residues K525, R528 (or Q528), and R531 (or Q531) and the COM of S2 helix. The restraint force constant was set at 16 kcal/mol/Å^2 during equilibration phase and was later reduced to 8 kcal/mol/Å^2 for the production phase. The collective variable and restraint potential were implemented using the Colvars module in NAMD3[97,98]. The temperature was maintained at 310 K using the Langevin thermostat, and pressure was held at 1 atm using the Nosé–Hoover Langevin piston method. Long-range electrostatics were treated using PME, and van der Waals interactions were truncated with a switching function from 10 to 12 Å. The final 5 ns of trajectory data from each window were used to reconstruct the potential of mean force (PMF) profile using the Weighted

Histogram Analysis Method (WHAM) (Grossfield's WHAM)[99,100], employing 50 bins along the reaction coordinate and a convergence tolerance of 0.0001 kcal/mol. Sufficient overlap between adjacent windows was verified to ensure reliable reconstruction of the free energy profile.

Statistics and Reproducibility

Statistical significance was assessed based on data parameters presented as the mean ± s.e.m. of n independent cells or patches. The two-sided Student's t-test was used for comparing two groups, while a one-way ANOVA followed by Tukey's post hoc test was employed for pairwise comparisons involving more than two data groups. Statistical significance was highlighted as $*p < 0.05$, $**p < 0.01$.

DATA AVAILABILITY

Source data are available as a Source Data File in figshare.com (doi: 10.6084/m9.figshare.28304378), and additional data are in the Supplementary Information. Please refer to https://doi.org/10.2210/pdb5VA1/pdb, https://doi.org/10.2210/pdb8EOW/pdb, https://doi.org/10.2210/pdb8EP0/pdb, and https://doi.org/10.2210/pdb8EP1/pdb for the PDB accession codes 5VA1, 8EOW, 8EP0, 8EP1 used in this paper.

CODE AVAILABILITY

Computational codes and models are available in figshare.com, doi:10.6084/m9.figshare.28304378.

ACKNOWLEGEMENT

We thank Natalie L. Macchi for technical support; Joel C. Eissenberg for editing the manuscript; Enrico Di Cera and Nicola Pozzi for feedback, E. James Petersson and Venkatesh Yarra (University of Pennsylvania) for sharing the noncanonical amino acid Acd and providing advice; Ryan A. Mehl (GCE4All Research Center, Oregon State University) for sharing the Acd RS1 aminoacyl tRNA synthetase and tRNA pair plasmid. This research is supported by National Institutes of Health (NIH) grants R35GM154778 (to G.D.) and R56HL169176 (to G.D. and E.T.). We gratefully acknowledge support from the Doisy Fund of the Edward A. Doisy Department of Biochemistry and Molecular Biology at Saint Louis University School of Medicine. In addition, the authors acknowledge funding from the NIH grant R24GM145965 (to E.T.) and National Science Foundation (NSF) QCB grant: 221835 (to E.T.). Computing resources were provided by the NSF ACCESS award: MCA06N060 (to E.T.).

AUTHOR CONTRIBUTIONS

G.D. conceived and designed the research. G.D. performed and analyzed fluorescence imaging experiments. L.J.H. performed patch-clamp recordings. L.J.H. and G.D. analyzed patch-clamp data. E.N.L. and G.D. performed molecular cloning of mutant hERG constructs. A.N.C, C.D.Q., E.T., and G.D. designed MD simulations. C.D.Q. performed and analyzed umbrella sampling of SMD simulations. A.N.C. performed and analyzed other MD simulations. E.T. supervised the MD simulations and analysis. G.D. wrote the manuscript with inputs from A.N.C, C.D.Q. and E.T.

COMPETING INTERESTS

The authors declare no competing interests.

REFERENCES

1 Hille, B. *Ion Channels of Excitable Membranes* 3rd edn, (Sinauer Associates, 2001).

2 Catterall, W. A., Wisedchaisri, G. & Zheng, N. The chemical basis for electrical signaling. *Nat Chem Biol* **13**, 455-463 (2017). https://doi.org:10.1038/nchembio.2353

3 Trudeau, M. C., Warmke, J. W., Ganetzky, B. & Robertson, G. A. HERG, a human inward rectifier in the voltage-gated potassium channel family. *Science* **269**, 92-95 (1995).

4 Ganetzky, B., Robertson, G. A., Wilson, G. F., Trudeau, M. C. & Titus, S. A. The eag family of K^+ channels in Drosophila and mammals. *Ann N Y Acad Sci* **868**, 356-369 (1999).

5 Anderson, C. L. *et al.* Large-scale mutational analysis of Kv11.1 reveals molecular insights into type 2 long QT syndrome. *Nat Commun* **5**, 5535 (2014). https://doi.org:10.1038/ncomms6535

6 Armstrong, C. M. & Bezanilla, F. Currents related to movement of the gating particles of the sodium channels. *Nature* **242**, 459-461 (1973). https://doi.org:10.1038/242459a0

7 Guo, J. *et al.* Structure of the voltage-gated two-pore channel TPC1 from Arabidopsis thaliana. *Nature* **531**, 196-201 (2016). https://doi.org:10.1038/nature16446

8 Xu, H. *et al.* Structural Basis of Nav1.7 Inhibition by a Gating-Modifier Spider Toxin. *Cell* **176**, 1238-1239 (2019). https://doi.org:10.1016/j.cell.2019.01.047

9 Wisedchaisri, G. *et al.* Resting-State Structure and Gating Mechanism of a Voltage-Gated Sodium Channel. *Cell* (2019). https://doi.org:10.1016/j.cell.2019.06.031

10 Dai, G., Aman, T. K., DiMaio, F. & Zagotta, W. N. The HCN channel voltage sensor undergoes a large downward motion during hyperpolarization. *Nat Struct Mol Biol* **26**, 686-694 (2019). https://doi.org:10.1038/s41594-019-0259-1

11 Dai, G., Aman, T. K., DiMaio, F. & Zagotta, W. N. Electromechanical coupling mechanism for activation and inactivation of an HCN channel. *Nat Commun* **12**, 2802 (2021). https://doi.org:10.1038/s41467-021-23062-7

12 Mandala, V. S. & MacKinnon, R. Voltage-sensor movements in the Eag Kv channel under an applied electric field. *Proc Natl Acad Sci U S A* **119**, e2214151119 (2022). https://doi.org:10.1073/pnas.2214151119

13 Mandala, V. S. & MacKinnon, R. The membrane electric field regulates the PIP_2-binding site to gate the KCNQ1 channel. *Proc Natl Acad Sci U S A* **120**, e2301985120 (2023). https://doi.org:10.1073/pnas.2301985120

14 Wang, W. & MacKinnon, R. Cryo-EM Structure of the Open Human Ether-a-go-go-Related K^+ Channel hERG. *Cell* **169**, 422-430 e410 (2017). https://doi.org:10.1016/j.cell.2017.03.048

15 Robertson, G. A. & Morais-Cabral, J. H. hERG Function in Light of Structure. *Biophys J* **118**, 790-797 (2020). https://doi.org:10.1016/j.bpj.2019.10.010

16 Long, S. B., Campbell, E. B. & Mackinnon, R. Voltage sensor of Kv1.2: structural basis of electromechanical coupling. *Science* **309**, 903-908 (2005). https://doi.org:10.1126/science.1116270

17 Long, S. B., Tao, X., Campbell, E. B. & MacKinnon, R. Atomic structure of a voltage-dependent K^+ channel in a lipid membrane-like environment. *Nature* **450**, 376-382 (2007). https://doi.org:10.1038/nature06265

18 Lee, C. H. & MacKinnon, R. Voltage Sensor Movements during Hyperpolarization in the HCN Channel. *Cell* **179**, 1582-1589 e1587 (2019). https://doi.org:10.1016/j.cell.2019.11.006

19 Han, S. *et al.* Cholesterol inhibits human voltage-gated proton channel hHv1. *Proc Natl Acad Sci U S A* **119**, e2205420119 (2022). https://doi.org:10.1073/pnas.2205420119

20 Han, S. *et al.* Structural dynamics determine voltage and pH gating in human voltage-gated proton channel. *Elife* **11** (2022). https://doi.org:10.7554/eLife.73093

21 Digman, M. A., Caiolfa, V. R., Zamai, M. & Gratton, E. The phasor approach to fluorescence lifetime imaging analysis. *Biophys J* **94**, L14-16 (2008). https://doi.org:10.1529/biophysj.107.120154

22 Hinde, E., Digman, M. A., Hahn, K. M. & Gratton, E. Millisecond spatiotemporal dynamics of FRET biosensors by the pair correlation function and the phasor approach to FLIM. *Proc Natl Acad Sci U S A* **110**, 135-140 (2013). https://doi.org:10.1073/pnas.1211882110
23 Zagotta, W. N. *et al.* An improved fluorescent noncanonical amino acid for measuring conformational distributions using time-resolved transition metal ion FRET. *Elife* **10** (2021). https://doi.org:10.7554/eLife.70236
24 Zagotta, W. N. *et al.* Measuring conformational equilibria in allosteric proteins with time-resolved tmFRET. *Biophys J* (2024). https://doi.org:10.1016/j.bpj.2024.01.033
25 Tao, X., Lee, A., Limapichat, W., Dougherty, D. A. & MacKinnon, R. A gating charge transfer center in voltage sensors. *Science* **328**, 67-73 (2010). https://doi.org:10.1126/science.1185954
26 McBride, C. M. *et al.* Mechanistic basis for type 2 long QT syndrome caused by KCNH2 mutations that disrupt conserved arginine residues in the voltage sensor. *J Membr Biol* **246**, 355-364 (2013). https://doi.org:10.1007/s00232-013-9539-6
27 Millat, G. *et al.* Spectrum of pathogenic mutations and associated polymorphisms in a cohort of 44 unrelated patients with long QT syndrome. *Clin Genet* **70**, 214-227 (2006). https://doi.org:10.1111/j.1399-0004.2006.00671.x
28 Waterhouse, A. *et al.* SWISS-MODEL: homology modelling of protein structures and complexes. *Nucleic Acids Res* **46**, W296-W303 (2018). https://doi.org:10.1093/nar/gky427
29 Choi, K. H., Song, C., Shin, D. & Park, S. hERG channel blockade by externally applied quaternary ammonium derivatives. *Biochim Biophys Acta* **1808**, 1560-1566 (2011). https://doi.org:10.1016/j.bbamem.2011.02.008
30 Codding, S. J. & Trudeau, M. C. The hERG potassium channel intrinsic ligand regulates N- and C-terminal interactions and channel closure. *J Gen Physiol* **151**, 478-488 (2019). https://doi.org:10.1085/jgp.201812129
31 Herzberg, I. M., Trudeau, M. C. & Robertson, G. A. Transfer of rapid inactivation and sensitivity to the class III antiarrhythmic drug E-4031 from HERG to M-eag channels. *J Physiol* **511 (Pt 1)**, 3-14 (1998). https://doi.org:10.1111/j.1469-7793.1998.003bi.x
32 Lau, C. H. Y. *et al.* Potassium dependent structural changes in the selectivity filter of HERG potassium channels. *Nat Commun* **15**, 7470 (2024). https://doi.org:10.1038/s41467-024-51208-w
33 Zhang, M., Liu, J. & Tseng, G. N. Gating charges in the activation and inactivation processes of the HERG channel. *J Gen Physiol* **124**, 703-718 (2004). https://doi.org:10.1085/jgp.200409119
34 Smith, P. L. & Yellen, G. Fast and slow voltage sensor movements in HERG potassium channels. *J Gen Physiol* **119**, 275-293 (2002). https://doi.org:10.1085/jgp.20028534
35 Zhang, M. *et al.* Interactions between charged residues in the transmembrane segments of the voltage-sensing domain in the hERG channel. *J Membr Biol* **207**, 169-181 (2005). https://doi.org:10.1007/s00232-005-0812-1
36 Aggarwal, S. K. & MacKinnon, R. Contribution of the S4 segment to gating charge in the Shaker K^+ channel. *Neuron* **16**, 1169-1177 (1996). https://doi.org:10.1016/s0896-6273(00)80143-9
37 Zagotta, W. N., Hoshi, T., Dittman, J. & Aldrich, R. W. Shaker potassium channel gating. II: Transitions in the activation pathway. *J Gen Physiol* **103**, 279-319 (1994). https://doi.org:10.1085/jgp.103.2.279
38 Handlin, L. J. & Dai, G. Direct regulation of the voltage sensor of HCN channels by membrane lipid compartmentalization. *Nat Commun* **14**, 6595 (2023). https://doi.org:10.1038/s41467-023-42363-7
39 Jones, C. M. *et al.* Genetic encoding of a highly photostable, long lifetime fluorescent amino acid for imaging in mammalian cells. *Chem Sci* **12**, 11955-11964 (2021). https://doi.org:10.1039/d1sc01914g
40 Avila-Crump, S. *et al.* Generating Efficient Methanomethylophilus alvus Pyrrolysyl-tRNA Synthetases for Structurally Diverse Non-Canonical Amino Acids. *ACS Chem Biol* **17**, 3458-3469 (2022). https://doi.org:10.1021/acschembio.2c00639

41 Meineke, B., Heimgartner, J., Eirich, J., Landreh, M. & Elsasser, S. J. Site-Specific Incorporation of Two ncAAs for Two-Color Bioorthogonal Labeling and Crosslinking of Proteins on Live Mammalian Cells. *Cell Rep* **31**, 107811 (2020). https://doi.org:10.1016/j.celrep.2020.107811
42 Horrocks, W. D., Jr., Holmquist, B. & Vallee, B. L. Energy transfer between terbium (III) and cobalt (II) in thermolysin: a new class of metal--metal distance probes. *Proc Natl Acad Sci U S A* **72**, 4764-4768 (1975).
43 Taraska, J. W., Puljung, M. C., Olivier, N. B., Flynn, G. E. & Zagotta, W. N. Mapping the structure and conformational movements of proteins with transition metal ion FRET. *Nat Methods* **6**, 532-537 (2009). https://doi.org:10.1038/nmeth.1341
44 Zagotta, W. N., Gordon, M. T., Senning, E. N., Munari, M. A. & Gordon, S. E. Measuring distances between TRPV1 and the plasma membrane using a noncanonical amino acid and transition metal ion FRET. *J Gen Physiol* **147**, 201-216 (2016). https://doi.org:10.1085/jgp.201511531
45 Dai, G. & Zagotta, W. N. Molecular mechanism of voltage-dependent potentiation of KCNH potassium channels. *Elife* **6** (2017). https://doi.org:10.7554/eLife.26355
46 Malacrida, L., Ranjit, S., Jameson, D. M. & Gratton, E. The Phasor Plot: A Universal Circle to Advance Fluorescence Lifetime Analysis and Interpretation. *Annu Rev Biophys* **50**, 575-593 (2021). https://doi.org:10.1146/annurev-biophys-062920-063631
47 Ranjit, S., Malacrida, L., Jameson, D. M. & Gratton, E. Fit-free analysis of fluorescence lifetime imaging data using the phasor approach. *Nat Protoc* **13**, 1979-2004 (2018). https://doi.org:10.1038/s41596-018-0026-5
48 Kucka, M. *et al.* Dependence of multidrug resistance protein-mediated cyclic nucleotide efflux on the background sodium conductance. *Mol Pharmacol* **77**, 270-279 (2010). https://doi.org:10.1124/mol.109.059386
49 Tristani-Firouzi, M., Chen, J. & Sanguinetti, M. C. Interactions between S4-S5 linker and S6 transmembrane domain modulate gating of HERG K+ channels. *J Biol Chem* **277**, 18994-19000 (2002). https://doi.org:10.1074/jbc.M200410200
50 Kasimova, M. A. *et al.* Helix breaking transition in the S4 of HCN channel is critical for hyperpolarization-dependent gating. *Elife* **8** (2019). https://doi.org:10.7554/eLife.53400
51 Vallmitjana, A. *et al.* Resolution of 4 components in the same pixel in FLIM images using the phasor approach. *Methods Appl Fluoresc* **8**, 035001 (2020). https://doi.org:10.1088/2050-6120/ab8570
52 Vallmitjana, A., Torrado, B., Dvornikov, A., Ranjit, S. & Gratton, E. Blind Resolution of Lifetime Components in Individual Pixels of Fluorescence Lifetime Images Using the Phasor Approach. *J Phys Chem B* **124**, 10126-10137 (2020). https://doi.org:10.1021/acs.jpcb.0c06946
53 Eggan, P., Gordon, S. E. & Zagotta, W. N. Ligand-coupled conformational changes in a cyclic nucleotide-gated ion channel revealed by time-resolved transition metal ion FRET. *Elife* **13** (2024). https://doi.org:10.7554/eLife.99854
54 Roux, B. The membrane potential and its representation by a constant electric field in computer simulations. *Biophys J* **95**, 4205-4216 (2008). https://doi.org:10.1529/biophysj.108.136499
55 Lorinczi, E. *et al.* Voltage-dependent gating of KCNH potassium channels lacking a covalent link between voltage-sensing and pore domains. *Nat Commun* **6**, 6672 (2015). https://doi.org:10.1038/ncomms7672
56 Whicher, J. R. & MacKinnon, R. Regulation of Eag1 gating by its intracellular domains. *Elife* **8** (2019). https://doi.org:10.7554/eLife.49188
57 Moradi, M. & Tajkhorshid, E. Mechanistic picture for conformational transition of a membrane transporter at atomic resolution. *Proc Natl Acad Sci U S A* **110**, 18916-18921 (2013). https://doi.org:10.1073/pnas.1313202110
58 Moradi, M. & Tajkhorshid, E. Computational Recipe for Efficient Description of Large-Scale Conformational Changes in Biomolecular Systems. *J Chem Theory Comput* **10**, 2866-2880 (2014). https://doi.org:10.1021/ct5002285

59 Moradi, M., Enkavi, G. & Tajkhorshid, E. Atomic-level characterization of transport cycle thermodynamics in the glycerol-3-phosphate:phosphate antiporter. *Nat Commun* **6**, 8393 (2015). https://doi.org:10.1038/ncomms9393
60 Liu, Z. *et al.* An LQT2-related mutation in the voltage-sensing domain is involved in switching the gating polarity of hERG. *BMC Biol* **22**, 29 (2024). https://doi.org:10.1186/s12915-024-01833-0
61 Zhu, F. & Hummer, G. Convergence and error estimation in free energy calculations using the weighted histogram analysis method. *J Comput Chem* **33**, 453-465 (2012). https://doi.org:10.1002/jcc.21989
62 Delemotte, L., Tarek, M., Klein, M. L., Amaral, C. & Treptow, W. Intermediate states of the Kv1.2 voltage sensor from atomistic molecular dynamics simulations. *Proc Natl Acad Sci U S A* **108**, 6109-6114 (2011). https://doi.org:10.1073/pnas.1102724108
63 Lacroix, J. J. *et al.* Intermediate state trapping of a voltage sensor. *J Gen Physiol* **140**, 635-652 (2012). https://doi.org:10.1085/jgp.201210827
64 Guo, S. C., Shen, R., Roux, B. & Dinner, A. R. Dynamics of activation in the voltage-sensing domain of Ciona intestinalis phosphatase Ci-VSP. *Nat Commun* **15**, 1408 (2024). https://doi.org:10.1038/s41467-024-45514-6
65 Villalba-Galea, C. A., Sandtner, W., Starace, D. M. & Bezanilla, F. S4-based voltage sensors have three major conformations. *Proc Natl Acad Sci U S A* **105**, 17600-17607 (2008). https://doi.org:10.1073/pnas.0807387105
66 Dickinson, M. S. *et al.* Molecular basis of multistep voltage activation in plant two-pore channel 1. *Proc Natl Acad Sci U S A* **119** (2022). https://doi.org:10.1073/pnas.2110936119
67 Wu, X., Ramentol, R., Perez, M. E., Noskov, S. Y. & Larsson, H. P. A second S4 movement opens hyperpolarization-activated HCN channels. *Proc Natl Acad Sci U S A* **118** (2021). https://doi.org:10.1073/pnas.2102036118
68 Moreau, A., Gosselin-Badaroudine, P., Boutjdir, M. & Chahine, M. Mutations in the Voltage Sensors of Domains I and II of Nav1.5 that are Associated with Arrhythmias and Dilated Cardiomyopathy Generate Gating Pore Currents. *Front Pharmacol* **6**, 301 (2015). https://doi.org:10.3389/fphar.2015.00301
69 Daniel, L. L. *et al.* SCN5A variant R222Q generated abnormal changes in cardiac sodium current and action potentials in murine myocytes and Purkinje cells. *Heart Rhythm* **16**, 1676-1685 (2019). https://doi.org:10.1016/j.hrthm.2019.05.017
70 Moreau, A. *et al.* A leaky voltage sensor domain of cardiac sodium channels causes arrhythmias associated with dilated cardiomyopathy. *Sci Rep* **8**, 13804 (2018). https://doi.org:10.1038/s41598-018-31772-0
71 Calloe, K. *et al.* Characterization and mechanisms of action of novel NaV1.5 channel mutations associated with Brugada syndrome. *Circ Arrhythm Electrophysiol* **6**, 177-184 (2013). https://doi.org:10.1161/CIRCEP.112.974220
72 James, Z. M. & Zagotta, W. N. Structural insights into the mechanisms of CNBD channel function. *J Gen Physiol* **150**, 225-244 (2018). https://doi.org:10.1085/jgp.201711898
73 Whicher, J. R. & MacKinnon, R. Structure of the voltage-gated K^+ channel EAG1 reveals an alternative voltage sensing mechanism. *Science* **353**, 664-669 (2016). https://doi.org:10.1126/science.aaf8070
74 Costa, F., Guardiani, C. & Giacomello, A. Molecular dynamics simulations suggest possible activation and deactivation pathways in the hERG channel. *Commun Biol* **5**, 165 (2022). https://doi.org:10.1038/s42003-022-03074-9
75 Moreau, A., Gosselin-Badaroudine, P. & Chahine, M. Molecular biology and biophysical properties of ion channel gating pores. *Q Rev Biophys* **47**, 364-388 (2014). https://doi.org:10.1017/S0033583514000109

76 Tombola, F., Pathak, M. M. & Isacoff, E. Y. Voltage-sensing arginines in a potassium channel permeate and occlude cation-selective pores. *Neuron* **45**, 379-388 (2005). https://doi.org:10.1016/j.neuron.2004.12.047
77 Vieira-Pires, R. S. & Morais-Cabral, J. H. 3_{10} helices in channels and other membrane proteins. *J Gen Physiol* **136**, 585-592 (2010). https://doi.org:10.1085/jgp.201010508
78 Infield, D. T. *et al.* Main-chain mutagenesis reveals intrahelical coupling in an ion channel voltage-sensor. *Nat Commun* **9**, 5055 (2018). https://doi.org:10.1038/s41467-018-07477-3
79 Burtscher, V. *et al.* Structural basis for hyperpolarization-dependent opening of human HCN1 channel. *Nat Commun* **15**, 5216 (2024). https://doi.org:10.1038/s41467-024-49599-x
80 Oliveira, B. L., Guo, Z. & Bernardes, G. J. L. Inverse electron demand Diels-Alder reactions in chemical biology. *Chem Soc Rev* **46**, 4895-4950 (2017). https://doi.org:10.1039/c7cs00184c
81 Jewett, J. C. & Bertozzi, C. R. Cu-free click cycloaddition reactions in chemical biology. *Chem Soc Rev* **39**, 1272-1279 (2010).
82 Dai, G. Neuronal KCNQ2/3 channels are recruited to lipid raft microdomains by palmitoylation of BACE1. *J Gen Physiol* **154** (2022). https://doi.org:10.1085/jgp.202112888
83 Dai, G., Yu, H., Kruse, M., Traynor-Kaplan, A. & Hille, B. Osmoregulatory inositol transporter SMIT1 modulates electrical activity by adjusting $PI(4,5)P_2$ levels. *Proc Natl Acad Sci U S A* **113**, E3290-3299 (2016). https://doi.org:10.1073/pnas.1606348113
84 Schmied, W. H., Elsasser, S. J., Uttamapinant, C. & Chin, J. W. Efficient multisite unnatural amino acid incorporation in mammalian cells via optimized pyrrolysyl tRNA synthetase/tRNA expression and engineered eRF1. *J Am Chem Soc* **136**, 15577-15583 (2014). https://doi.org:10.1021/ja5069728
85 Handlin, L. J. *et al.* Membrane Lipid Domains Modulate HCN Channels in Nociceptor DRG Neurons. *bioRxiv* (2024). https://doi.org:https://doi.org/10.1101/2023.09.02.556056
86 Gordon, S. E., Munari, M. & Zagotta, W. N. Visualizing conformational dynamics of proteins in solution and at the cell membrane. *Elife* **7** (2018). https://doi.org:10.7554/eLife.37248
87 Jumper, J. *et al.* Highly accurate protein structure prediction with AlphaFold. *Nature* **596**, 583-589 (2021). https://doi.org:10.1038/s41586-021-03819-2
88 Post, J. A., Verkleij, A. J. & Langer, G. A. Organization and function of sarcolemmal phospholipids in control and ischemic/reperfused cardiomyocytes. *J Mol Cell Cardiol* **27**, 749-760 (1995). https://doi.org:10.1016/0022-2828(95)90080-2
89 MacKerell, A. D. *et al.* All-atom empirical potential for molecular modeling and dynamics studies of proteins. *J Phys Chem B* **102**, 3586-3616 (1998). https://doi.org:10.1021/jp973084f
90 Phillips, J. C. *et al.* Scalable molecular dynamics with NAMD. *J Comput Chem* **26**, 1781-1802 (2005). https://doi.org:10.1002/jcc.20289
91 Phillips, J. C. *et al.* Scalable molecular dynamics on CPU and GPU architectures with NAMD. *J Chem Phys* **153**, 044130 (2020). https://doi.org:10.1063/5.0014475
92 Hoover, W. G. Canonical dynamics: Equilibrium phase-space distributions. *Phys Rev A Gen Phys* **31**, 1695-1697 (1985). https://doi.org:10.1103/physreva.31.1695
93 Feller, S. E., Zhang, Y. H., Pastor, R. W. & Brooks, B. R. Constant pressure molecular dynamics simulation: the Langevin piston method. *Journal of Chemical Physics* **103**, 4613-4621 (1995). https://doi.org:10.1063/1.470648
94 Martyna, G. J., Tobias, D. J. & Klein, M. L. Constant Pressure Molecular Dynamics Algorithms. *Journal of Chemical Physics* **101**, 4177-4189 (1994). https://doi.org:10.1063/1.467468
95 Pollock, E. L. & Glosli, J. Comments on P^3M, FMM, and the Ewald method for large periodic coulombic systems. *Computer Physics Communications* **95**, 93-110 (1996). https://doi.org:10.1016/0010-4655(96)00043-4
96 Torrie, G. M. & Valleau, J. P. Nonphysical sampling distributions in Monte Carlo free-energy estimation: Umbrella sampling. *Journal of Computational Physics* **23**, 187-199 (1977). https://doi.org:https://doi.org/10.1016/0021-9991(77)90121-8

97 Fiorin, G., Klein, M. L. & Hénin, J. Using collective variables to drive molecular dynamics simulations. *Mol Phys* **111**, 3345-3362 (2013). https://doi.org:10.1080/00268976.2013.813594

98 Fiorin, G. *et al.* Expanded Functionality and Portability for the Colvars Library. *Journal of Physical Chemistry B* **128**, 11108-11123 (2024). https://doi.org:10.1021/acs.jpcb.4c05604

99 Kumar, S., Bouzida, D., Swendsen, R. H., Kollman, P. A. & Rosenberg, J. M. The Weighted Histogram Analysis Method for Free-Energy Calculations on Biomolecules .1. The Method. *Journal of Computational Chemistry* **13**, 1011-1021 (1992). https://doi.org:DOI 10.1002/jcc.540130812

100 Grossfield, A. WHAM: the weighted histogram analysis method. (Version 2.1.0). https://doi.org:http://membrane.urmc.rochester.edu/wordpress/?page_id=126

FIGURE LEGENDS

Fig. 1. Design of phasor FLIM-tmFRET strategies for measuring voltage sensor movement in hERG channels.

a. Representative current traces for activation of WT+ hERG1 channels, elicited by steps of depolarizing voltage pulses from -120 mV to +100 mV. Tail currents were recorded at -100 mV. Also shown are representative current traces for activation of hERG1-R531Q+ channels, produced using the same voltage protocol. **b**. Comparison of conductance-voltage (G-V) relationships for activation of hERG WT+ and hERG-R531Q+ channels. **c**. Diagram illustrating the dual stop-codon (amber and ochre) suppression for incorporating Acd and ProK in a mutually orthogonal manner. **d**. Absorption and emission spectra showing the spectral overlap between the Acd emission incorporated to hERG channels (L523 site) and the molar absorption of Co^{2+} or Cu^{2+} coordinated with azido-DOTA. **e**. Design of a tmFRET pair with the FRET donor positioning in the L523TAG site of the S4 helix and the FRET acceptor in the C-terminal end of the S1 helix (near the S1-S2 linker). YFP not shown in the structural cartoon. **f**. Mono-exponential lifetime decay of Acd when incorporated into the L523 site. The lifetime species of membrane localized Acd can also be displayed in the phasor plot, with $\tau(\varphi)$ = 11.7 ns and $\tau(m)$ = 12.6 ns. The slight deviation of the Acd lifetime species from the universal semicircle is due to background contribution, typically 2% - 5%. **g**. FRET trajectory calculation enabled by the phasor plotting for $hERG_{tmFRET}$ channels, labeled with Cu^{2+} acceptor via CuAAC click chemistry in the presence of 120 mM extracellular KCl. The inset shows an amplified view. **h**. Similar FRET trajectory calculation for $hERG_{tmFRET}$-R531Q channels as a comparison. The red cursor covering the lifetime species is more distant from the green cursor of the donor alone, indicating greater FRET in this case. **i**. Summary data showing the apparent FRET efficiency of $hERG_{tmFRET}$ in regular PBS buffer (n = 7 cells) or with 120 mM KCl (n = 4 cells), and $hERG_{tmFRET}$-R531Q channels in PBS (n = 4) or high KCl (n = 8), using the FRET trajectory method as in panels g and h. Data shown are mean ± s.e.m., *p = 4e-5 at high KCl conditions using one-way ANOVA (no adjustment).

Fig. 2. Applying linear unmixing of phasor analysis to the FLIM-tmFRET for studying hERG channels.

a. Structural cartoons illustrating the low FRET state and high FRET state in the context of L523TAG/G439TAA FRET pair, corresponding to the homology models of hERG-VSD in the down and up states. Distances between the β carbon of L523 and the α carbon of G439, D(Cβ-Cα), are 29 Å and 19 Å in the down and up states, based on homology hERG models derived from cryo-EM structures of Eag channels. **b**. Representative linear unmixing approach to estimate the FRET efficiency corresponding to the high FRET state of $hERG_{tmFRET}$ channels at 120 mM KCl. The fitting is based on the pattern of lifetime distribution on the phasor plot. The red cursor points to a hypothetical scenario that 100% of voltage sensors are in the up position, and thus the high FRET state of 35%. The background contribution is 4% for the donor alone lifetime and 6% in the presence of the acceptor. The arrow points to the cursor of the lifetime associated with the high FRET-state if background contribution is absent. **c-d**. Representative phasor-based tmFRET analysis from individual cells expressing $hERG_{tmFRET}$ (c) and $hERG_{tmFRET}$-R531Q (d) channels, using the L523/G439 pair. FRET was measured under three conditions: NMDG (to induce membrane hyperpolarization), dPBS (reference condition), and 120 mM KCl (to induce membrane depolarization). In $hERG_{tmFRET}$ (c), FRET efficiency is similar across all conditions, whereas in $hERG_{tmFRET}$-R531Q (d), distinct FRET efficiencies are observed. **e-g**. Summary data showing FRET efficiencies (e), estimated donor-acceptor distances (f), and the fraction of the high FRET state (g), calculated via linear unmixing using the phasor approach. For $hERG_{tmFRET}$-R531Q, statistical comparisons of FRET efficiency and distance yielded p = 0.03 (NMDG vs dPBS), p = 3.5e-13 (NMDG vs KCl), and p = 3.8e-13 (dPBS vs KCl), by one-way ANOVA (no adjustment). For $hERG_{tmFRET}$, statistical comparisons of the percentage of FRET yielded p = 0.2 (NMDG vs dPBS), p = 1.4e-7 (NMDG vs KCl) and and p = 3e-6 (dPBS vs KCl). Sample sizes: $hERG_{tmFRET}$: NMDG (n = 6 cells), dPBS (n = 10 cells),

KCl (n = 4 cells); $hERG_{tmFRET}$-R531Q: NMDG (n = 5), dPBS (n = 7), KCl (n = 8). Data are presented as mean ± s.e.m.

Fig. 3. Alternative tmFRET pairs yielded similar intermediate distances in the hERG-R531Q channel.
a. Structural cartoon illustrating the four different tmFRET pairs, L523TAG as the donor and A430TAA, T436TAA, G439TAA, P440TAA as acceptors. **b**. Representative phasor analysis showing the different FRET efficiencies comparing the L523TAG/T436TAA and L523TAG/P440TAA pairs. Cells are imaged in the 120 mM KCl depolarizing condition. **c**. Summary of donor-acceptor distance estimates calculated from measured tmFRET of the four pairs in the depolarizing (high KCl) condition, n = 5 cells for A430, n = 3 cells for T436, n = 4 cells for G439, and n = 5 cells for A440. One-way ANOVA (no adjustment) showed statistical significance between all pair-wise comparisons, particularly p = 4e-3 (A430 vs T436), p = 5e-4 (A430 vs G439), p = 4e-3 (G439 vs P440). **d**. Representative phasor-plot analysis of the L523/P440 tmFRET from individual cells for $hERG_{tmFRET}$ (control) and $hERG_{tmFRET}$-R531Q channels under various conditions. **e-g**. Summary data showing FRET efficiencies of $hERG_{tmFRET}$-L523/P440 pair (e), estimated donor-acceptor distances (f), and the fraction of the high FRET state (g). Data shown are presented as mean ± s.e.m. For FRET efficiencies and estimated distances of R531Q, p = 0.025 (NMDG vs dPBS), p = 1.3e-9 (NMDG vs KCl), and p = 2.1e-8 (dPBS vs KCl), one-way ANOVA (no adjustment). For the percentage of FRET state of $hERG_{tmFRET}$-L523/P440, p = 0.024 (NMDG vs dPBS), p = 7.8e-96 (NMDG vs KCl), and p = 1e-4 (dPBS vs KCl), one-way ANOVA (no adjustment). Sample sizes: $hERG_{tmFRET}$: NMDG (n = 3 cells), dPBS (n = 4 cells), KCl (n = 5 cells); $hERG_{tmFRET}$-R531Q: NMDG (n = 6), dPBS (n = 6), KCl (n = 5).

Fig. 4. R531Q induces displacement and increased tilt of the S4 helix in MD simulations.
a. MD simulation of the full-length hERG-R531Q tetramer showing the S4 helix in an elevated and tilted conformation compared to the hERG-WT tetramer. A close-up view of the S4 helix is shown for one representative subunit. Similar R531Q-induced conformational changes in the S4 helix were observed in simulations of hERG transmembrane-domain monomers. **b**. Comparison of tmFRET-estimated distances in $hERG_{tmFRET}$-R531Q channels between the intermediate FRET state and the high FRET state for two FRET pairs (G439/L523 and P440/L523). These distances were compared to Cα–Cα distances of the corresponding residue pairs derived from MD simulation-based homology models. **c**-**d**. Representative snapshots of hERG-WT-VSD conformations (c) and hERG-R531Q-VSD conformations (d) captured along the trajectory of steered MD-induced S4 rearrangement. Membrane lipid head groups are depicted as yellow spheres. **e.** Time course of the distance of the center of mass (COM) of the R528 side chain in the WT and the R531Q mutant, measured relative to the COM of a reference residue, F463, during the SMD simulation. **f.** Time course of the distance between COM of the Q531 side chain and COM of the F463 side chain in the R531Q mutant, along with the corresponding distance in the WT, over the course of the SMD trajectory. **g**. Time course of the average combined distance between the Cβ atoms of residues 525, 528, and 531 in the R528Q mutant and the WT, measured relative to the COM of the S2 helix during the SMD simulation.

Fig. 5. Distinct S4 conformations induced by R528Q suggested by FLIM-tmFRET and MD simulations.
a-c. Representative analysis of the hERG from individual cells, when R528Q was included. **d**. Summary data of the estimated FRET efficiencies and percentage of the FRET state using linear unmixing of the phasor approach. Data shown are presented as mean ± s.e.m., Sample sizes: NMDG (n = 5 cells), dPBS (n = 5 cells), KCl (n = 6 cells). For the FRET efficiency, p =1e-6 between NMDG and KCl conditions, and p = 8e-6 between PBS and KCl conditions, one-way ANOVA (no adjustment). For the percentage of FRET

state, p =0.01 between NMDG and dPBS conditions, p = 1.4e-5 between NMDG and KCl conditions, p =0.005 between dPBS and KCl conditions. **e**. Representative snapshots of hERG-R528Q-VSD conformations captured along the trajectory of steered MD-induced S4 rearrangement. Membrane lipid head groups are depicted as yellow spheres. **f.** Time course of the distance of the center of mass (COM) of the Q528 side chain in the R528Q mutant and COM of the R528 side chain in the WT, measured relative to the COM of a reference residue, F463, during the SMD simulation. **g.** Time course of the distance between COM of the R531 side chain and COM of the F463 side chain in the R528Q mutant, along with the corresponding distance in the WT, over the course of the SMD trajectory. **h**. Time course of the average combined distance between the Cβ atoms of residues 525, 528, and 531 in the R528Q mutant and the WT, measured relative to the COM of the S2 helix, during the SMD simulation.

Fig. 6. Conformational free energy landscape of S4 movement in WT, R531Q, and R528Q hERG channels.

a-**c**. One-dimensional potential of mean force (PMF) profiles for the monomer transmembrane domains of WT (a), R531Q (b), and R528Q (c) derived from steered molecular dynamics simulations. The profiles depict free energy minima along the collective displacement of residues 525, 528, and 531 (collective variables) as the S4 segment transitions from the intermediate I to the up conformation. Free energy minima are highlighted by red triangles.

d. Schematic representations of the VSD topology and associated charge interactions in the down, intermediate I, intermediate II, and up states. The intermediate I conformation differs between the WT and the R531Q or R528Q mutants. The intermediate II is most stable in the R528Q mutant.

Figure 1

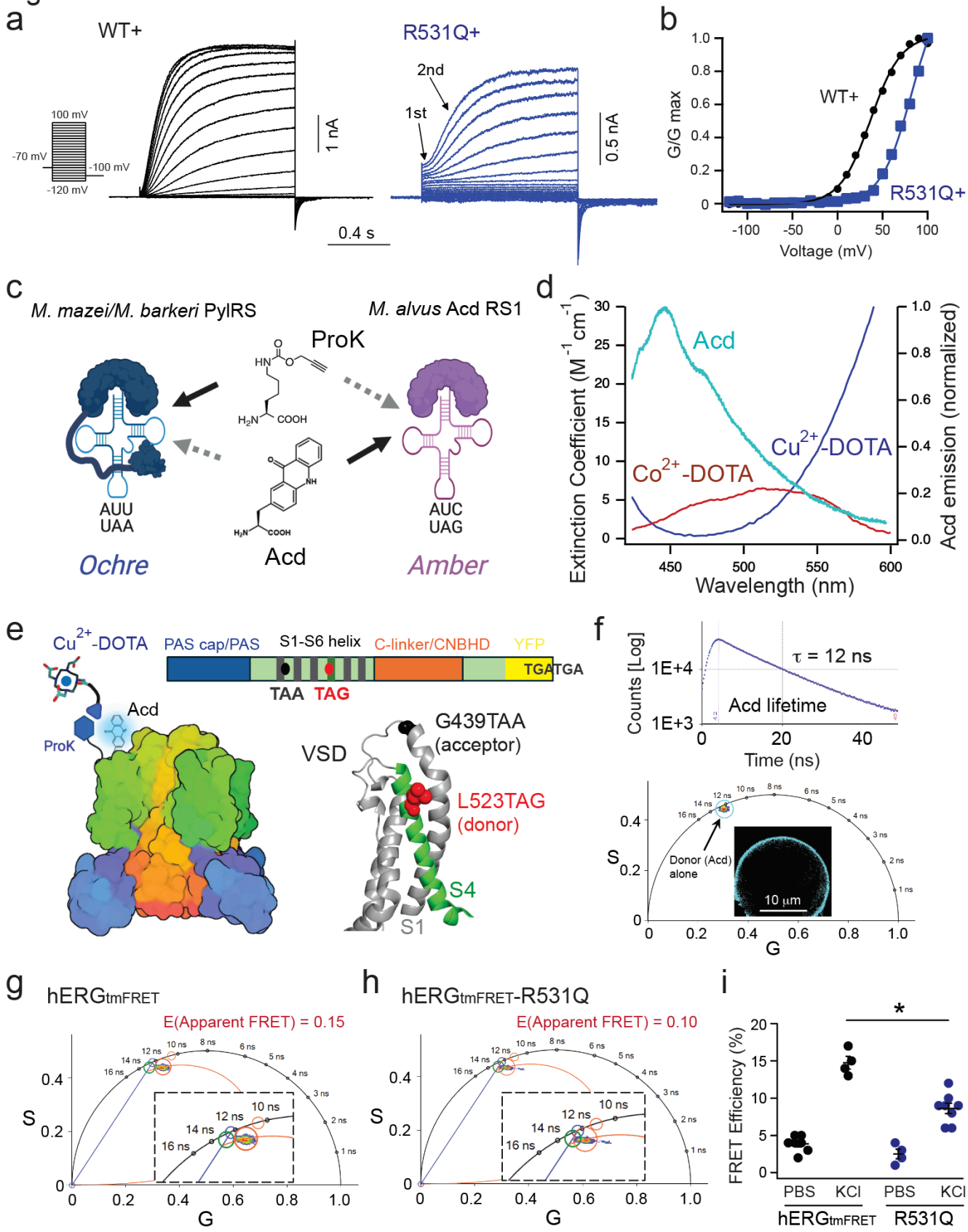
a
WT+
R531Q+
100 mV
-70 mV
-100 mV
-120 mV
1 nA
0.4 s
2nd
1st
0.5 nA
b
G/G max
WT+
R531Q+
Voltage (mV)
c
M. mazei/M. barkeri PylRS
M. alvus Acd RS1
ProK
AUU
UAA
Ochre
Acd
AUC
UAG
Amber
d
Extinction Coefficient (M-1 cm-1)
Acd emission (normalized)
Acd
Cu2+-DOTA
Co2+-DOTA
Wavelength (nm)
e
Cu2+-DOTA
PAS cap/PAS
S1-S6 helix
C-linker/CNBHD
YFP
TGATGA
TAA
TAG
Acd
ProK
VSD
G439TAA
(acceptor)
L523TAG
(donor)
S4
S1
f
Counts [Log]
τ = 12 ns
Acd lifetime
Time (ns)
Donor (Acd)
alone
10 μm
S
G
g
hERGtmFRET
E(Apparent FRET) = 0.15
h
hERGtmFRET-R531Q
E(Apparent FRET) = 0.10
i
FRET Efficiency (%)
PBS
KCl
PBS
KCl
hERGtmFRET
R531Q

Figure 2

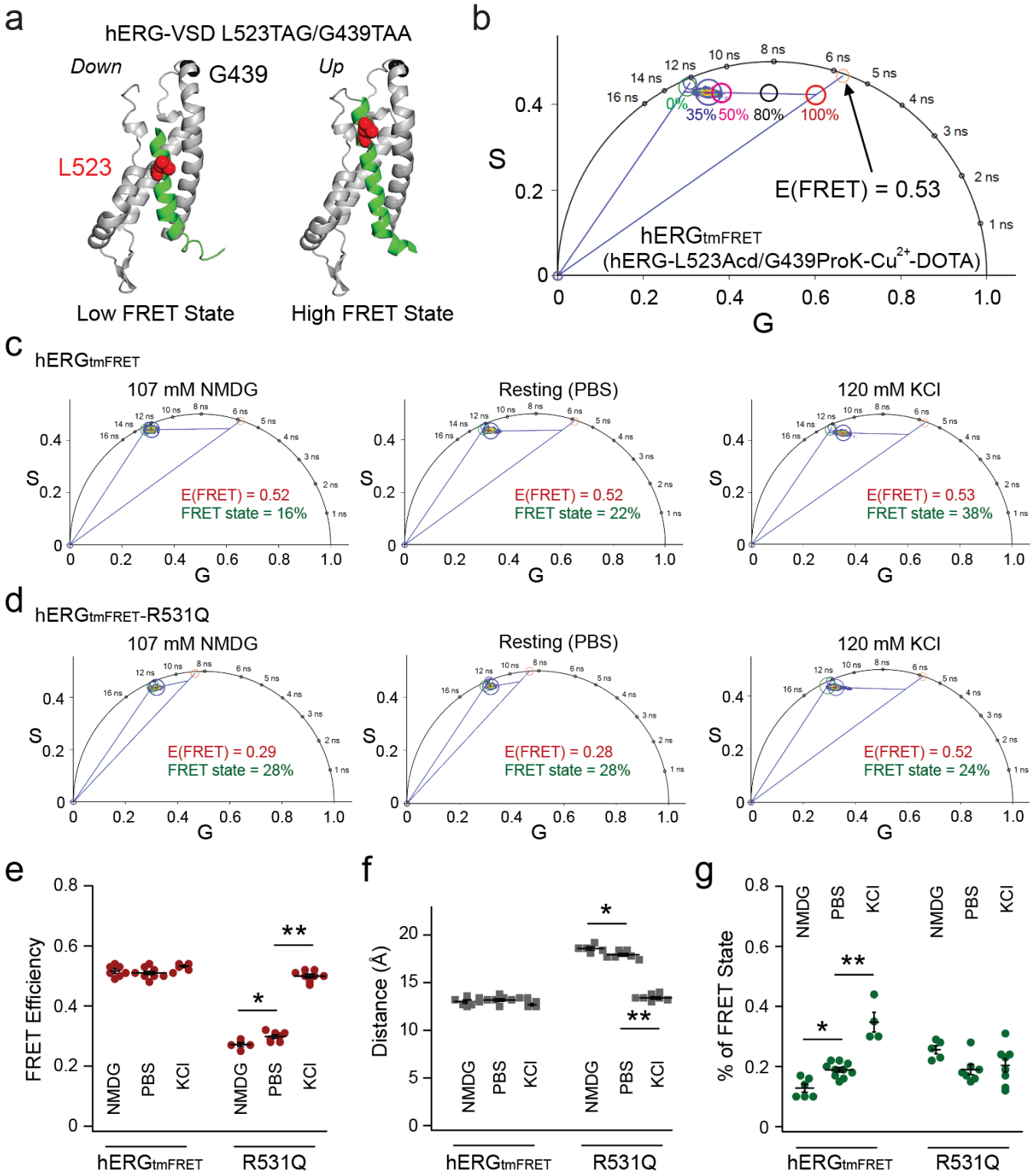
a
hERG-VSD L523TAG/G439TAA
Down
G439
Up
L523
Low FRET State
High FRET State
b
S
G
E(FRET) = 0.53
hERGtmFRET
(hERG-L523Acd/G439ProK-Cu2+-DOTA)
0%
35%
50%
80%
100%
c
hERGtmFRET
107 mM NMDG
E(FRET) = 0.52
FRET state = 16%
Resting (PBS)
E(FRET) = 0.52
FRET state = 22%
120 mM KCl
E(FRET) = 0.53
FRET state = 38%
d
hERGtmFRET-R531Q
107 mM NMDG
E(FRET) = 0.29
FRET state = 28%
Resting (PBS)
E(FRET) = 0.28
FRET state = 28%
120 mM KCl
E(FRET) = 0.52
FRET state = 24%
e
FRET Efficiency
NMDG
PBS
KCl
hERGtmFRET
R531Q
f
Distance (Å)
g
% of FRET State

Figure 3

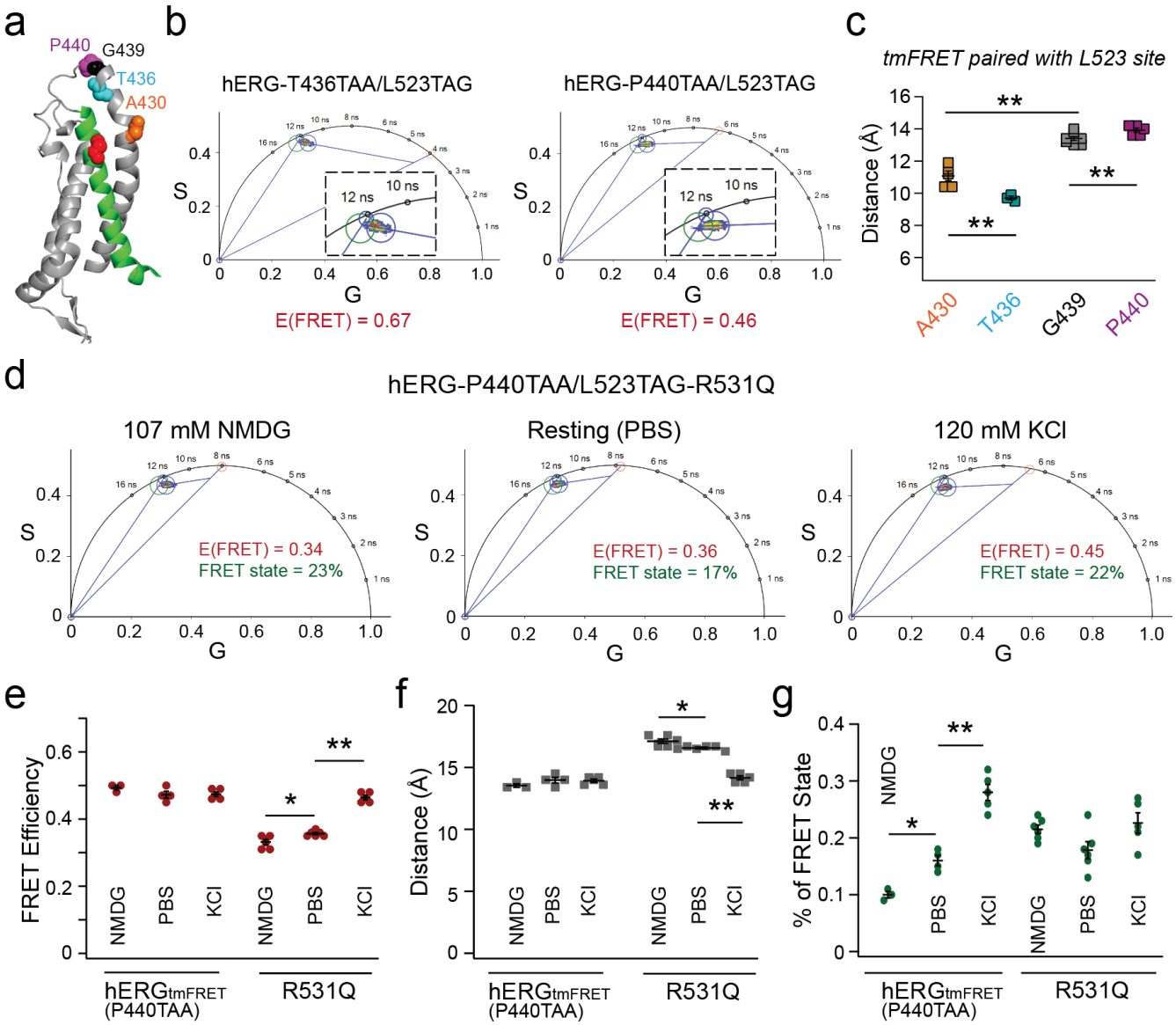
a
P440
G439
T436
A430
b
hERG-T436TAA/L523TAG
hERG-P440TAA/L523TAG
S
G
12 ns
10 ns
E(FRET) = 0.67
E(FRET) = 0.46
c
tmFRET paired with L523 site
Distance (Å)
A430
T436
G439
P440
d
hERG-P440TAA/L523TAG-R531Q
107 mM NMDG
Resting (PBS)
120 mM KCl
E(FRET) = 0.34
FRET state = 23%
E(FRET) = 0.36
FRET state = 17%
E(FRET) = 0.45
FRET state = 22%
e
FRET Efficiency
NMDG
PBS
KCl
hERGtmFRET (P440TAA)
R531Q
f
Distance (Å)
g
% of FRET State

Figure 4

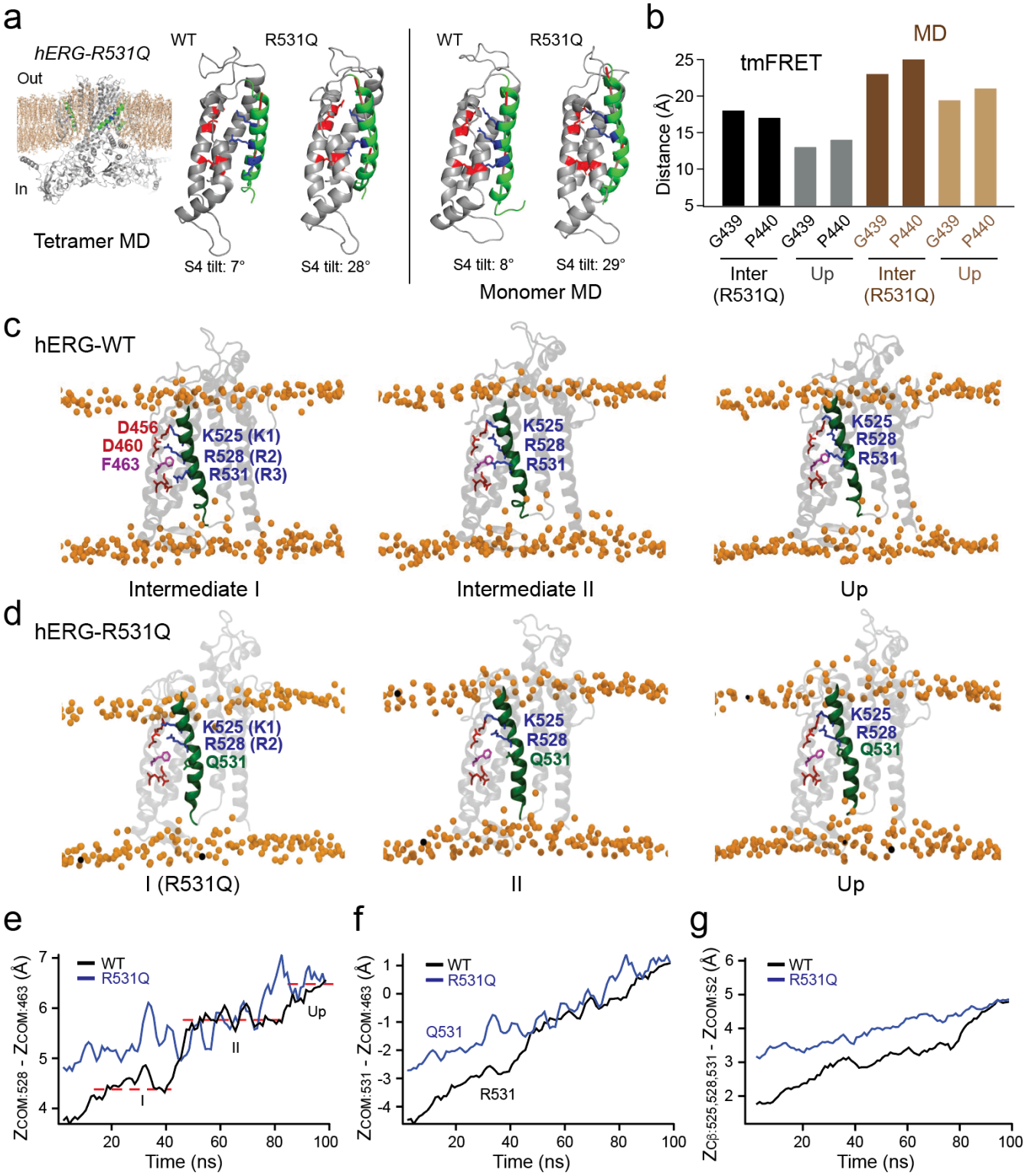
a
hERG-R531Q
Out
In
Tetramer MD
WT
R531Q
S4 tilt: 7°
S4 tilt: 28°
WT
R531Q
S4 tilt: 8°
S4 tilt: 29°
Monomer MD
b
tmFRET
MD
Distance (Å)
25
20
15
10
5
G439
P440
G439
P440
G439
P440
G439
P440
Inter (R531Q)
Up
Inter (R531Q)
Up
c
hERG-WT
D456
D460
F463
K525 (K1)
R528 (R2)
R531 (R3)
K525
R528
R531
K525
R528
R531
Intermediate I
Intermediate II
Up
d
hERG-R531Q
K525 (K1)
R528 (R2)
Q531
K525
R528
Q531
K525
R528
Q531
I (R531Q)
II
Up
e
WT
R531Q
I
II
Up
ZCOM:528 - ZCOM:463 (Å)
Time (ns)
f
WT
R531Q
Q531
R531
ZCOM:531 - ZCOM:463 (Å)
Time (ns)
g
WT
R531Q
ZCβ:525,528,531 - ZCOM:S2 (Å)
Time (ns)

Figure 5

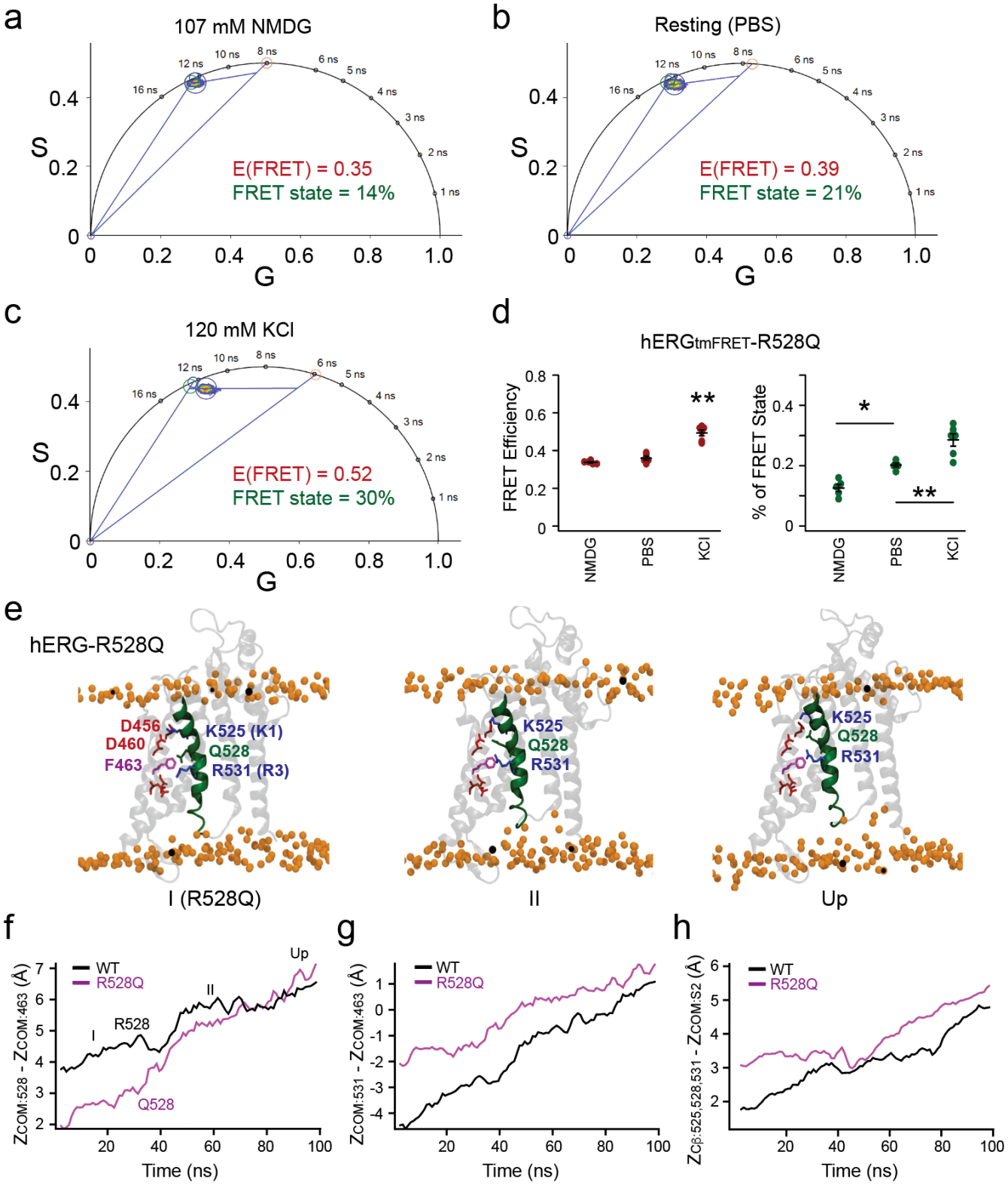
a
107 mM NMDG
E(FRET) = 0.35
FRET state = 14%
b
Resting (PBS)
E(FRET) = 0.39
FRET state = 21%
c
120 mM KCl
E(FRET) = 0.52
FRET state = 30%
S
G
16 ns
12 ns
10 ns
8 ns
6 ns
5 ns
4 ns
3 ns
2 ns
1 ns
d
hERGtmFRET-R528Q
FRET Efficiency
% of FRET State
NMDG
PBS
KCl
e
hERG-R528Q
D456
D460
F463
K525 (K1)
Q528
R531 (R3)
K525
Q528
R531
K525
Q528
R531
I (R528Q)
II
Up
f
WT
R528Q
R528
Q528
I
II
Up
ZCOM:528 - ZCOM:463 (Å)
Time (ns)
g
ZCOM:531 - ZCOM:463 (Å)
Time (ns)
h
ZCβ:525,528,531 - ZCOM:S2 (Å)
Time (ns)

Figure 6

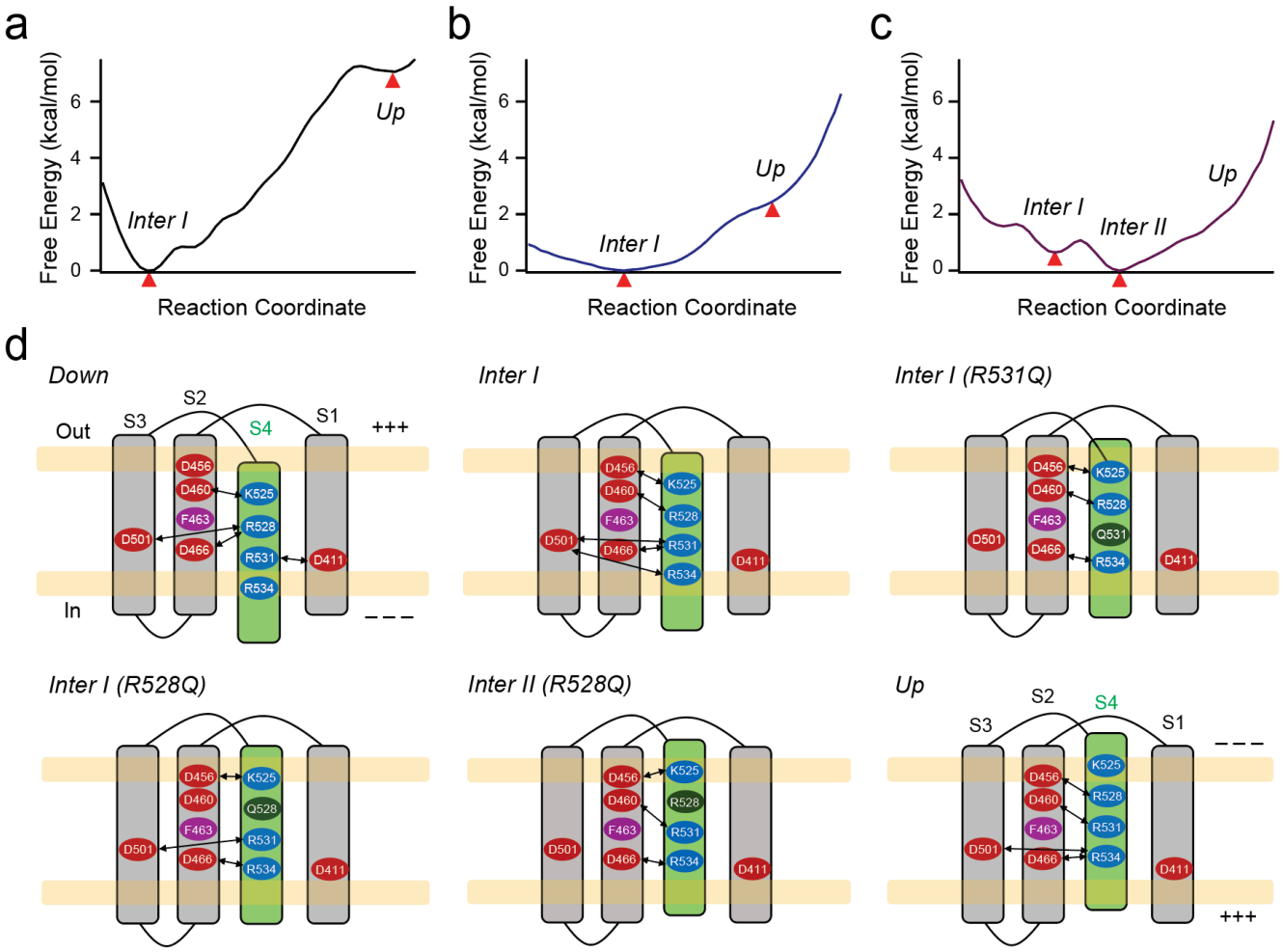
a
Free Energy (kcal/mol)
0
2
4
6
Inter I
Up
Reaction Coordinate
b
Free Energy (kcal/mol)
0
2
4
6
Inter I
Up
Reaction Coordinate
c
Free Energy (kcal/mol)
0
2
4
6
Inter I
Inter II
Up
Reaction Coordinate
d
Down
Out
In
S3
S2
S4
S1
+++
– – –
D456
D460
F463
D466
D501
D411
K525
R528
R531
R534
Q528
Q531
Inter I
Inter I (R531Q)
Inter I (R528Q)
Inter II (R528Q)
Up